The Astrophysical Journal, 961:118 (22pp), 2024 January 20 https://doi.org/10.3847/1538-4357/ad0c4e

A Census of Star Formation Histories of Massive Galaxies at $0.6 < z < 1$ from Spectrophotometric Modeling Using Bagpipes and Prospector

Yasha Kaushal[1], Angelos Nersesian[2], Rachel Bezanson[1], Arjen van der Wel[2], Joel Leja[3,4,5], Adam Carnall[6], Anna Gallazzi[7], Stefano Zibetti[7], Gourav Khullar[1], Marijn Franx[8], Adam Muzzin[9], Anna de Graaff[8,10], Camilla Pacifici[11], Katherine E. Whitaker[12,13], Eric F. Bell[14], and Marco Martorano[2]

[1] Department of Physics and Astronomy and PITT PACC, University of Pittsburgh, 3941 O'Hara Street, Pittsburgh, PA 15213, USA
[2] Sterrenkundig Observatorium, Universiteit Gent, Krijgslaan 281 S9, B-9000 Gent, Belgium
[3] Department of Astronomy & Astrophysics, The Pennsylvania State University, University Park, PA 16802, USA
[4] Institute for Computational & Data Sciences, The Pennsylvania State University, University Park, PA 16802, USA
[5] Institute for Gravitation and the Cosmos, The Pennsylvania State University, University Park, PA 16802, USA
[6] Institute for Astronomy, School of Physics and Astronomy, University of Edinburgh, Royal Observatory, Edinburgh, EH9 3HJ, UK
[7] INAF-Osservatorio Astrofisico di Arcetri, Largo Enrico Fermi 5, I-50125 Firenze, Italy
[8] Leiden Observatory, Leiden University, P.O. Box 9513, NL-2300 AA Leiden, The Netherlands
[9] Department of Physics and Astronomy, York University, 4700 Keele Street, Toronto, Ontario, M3J 1P3, Canada
[10] Max-Planck-Institut für Astronomie, Königstuhl 17, D-69117, Heidelberg, Germany
[11] Space Telescope Science Institute, 3700 San Martin Drive, Baltimore, MD 21218, USA
[12] Department of Astronomy, University of Massachusetts, Amherst, MA 01003, USA
[13] Cosmic Dawn Center (DAWN), Niels Bohr Institute, University of Copenhagen, Jagtvej 128, København N, DK-2200, Denmark
[14] Department of Astronomy, University of Michigan, Ann Arbor, MI 48109, USA

Received 2023 July 5; revised 2023 October 23; accepted 2023 November 8; published 2024 January 18

Abstract

We present individual star formation histories (SFHs) of ~3000 massive galaxies ($\log(M_*/M_\odot) > 10.5$) from the Large Early Galaxy Astrophysics Census spectroscopic survey at a lookback time of ~7 billion yr and quantify the population trends leveraging 20 hr deep-integrated spectra of these ~1800 star-forming and ~1200 quiescent galaxies at $0.6 < z < 1.0$. Essentially all galaxies at this epoch contain stars of age <3 Gyr, in contrast with older massive galaxies today, facilitating better recovery of previous generations of star formation at cosmic noon and earlier. We conduct spectrophotometric analysis using parametric and nonparametric Bayesian stellar population synthesis modeling tools—`Bagpipes` and `Prospector`—to constrain the median SFHs of this mass complete sample and characterize population trends. A consistent picture arises for the late-time stellar mass growth when quantified as t_{50} and t_{90}, corresponding to the age of the Universe when galaxies formed 50% and 90% of their total stellar mass, although the two methods disagree at the earliest formation times (e.g., t_{10}). Our results reveal trends in both stellar mass and stellar velocity dispersion as in the local Universe—low-mass galaxies with shallower potential wells grow their stellar masses later in cosmic history compared to high-mass galaxies. Unlike local quiescent galaxies, the median duration of late-time star formation ($\tau_{\rm SF,late} = t_{90}$–$t_{50}$) does not consistently depend on the stellar mass. This census sets a benchmark for future deep spectrophotometric studies of the more distant Universe.

Unified Astronomy Thesaurus concepts: Galaxy evolution (594); Galaxy formation (595); Galaxy stellar content (621); Galaxy spectroscopy (2171); Galaxy photometry (611); Bayesian statistics (1900); Star formation (1569)

Supporting material: machine-readable tables

1. Introduction

Galaxies are complex systems of multiple stellar populations. Observational constraints on the timescales of star formation and hence stellar mass growth and assembly enable us to understand the role of various physical mechanisms and their environment in guiding the formation and cosmic evolution of galaxies (Panter et al. 2007; Leitner 2012). Understanding these processes on various physical scales (radial and spatially resolved) and temporal scales also helps shed light on some of the long-standing puzzles, such as when and how galaxies stop forming stars (quenching) (Schawinski et al. 2014; Schreiber et al. 2016; Wild et al. 2016; Carnall et al. 2018; Maltby et al. 2018) and the transition from star forming to quiescence that leaves a bimodal population (Bell et al. 2004; Muzzin et al. 2013; Vulcani et al. 2014; Smethurst et al. 2015; Taylor et al. 2015).

Our current knowledge of the formation and cosmic evolution of galaxies is fundamentally limited by trade-offs between the quality and quantity of observations. Building a coherent picture of galaxy evolution demands (a) looking back in time for galaxies in the younger Universe without compromising the quality of observations, and (b) a statistically large representative sample size to connect the dots between similar populations of galaxies at multiple epochs. This is difficult owing to technological and observational challenges as light from galaxies at increasing distances dims and shifts to a less accessible infrared regime.

As stellar sources predominantly emit in the UV/optical to near-IR wavelengths, broadband multiwavelength spectral energy distribution (SED) of a galaxy contains information about its total stellar mass and dust reddening. Stellar population synthesis (SPS) modeling is a widely used technique to derive physical properties (e.g., age, mass, dust, metallicity) of a composite stellar population (often a galaxy). This modeling is often limited to broadband photometric data due to its relative availability and the speed and simplicity of modeling a handful of data points compared to modeling a higher-resolution spectrum. However, broadband photometry itself may not be sufficient to completely break the dust-age–metallicity degeneracy or to constrain higher-order moments of star formation histories (SFHs) (Leja et al. 2017, 2019; Tacchella et al. 2022; Nersesian et al. 2023). The numerous, old low-mass stars have long lifetimes and slow spectral evolution, yet leave weak imprints on observed data owing to their faint intrinsic luminosities. Therefore, inferring SFHs from photometry only is strongly susceptible to even small perturbations in data, leading to the different recovery of SFHs (see e.g., Ocvirk et al. 2006). The recovered SFHs from mocks show biases up to 0.2 dex in the mass-weighted formation times. This is even worse with real-world broadband photometric data having more systematic uncertainties involved (Carnall et al. 2019a; Leja et al. 2019). Photometry alone is not always sufficient to differentiate among modeling assumptions (Belli et al. 2018; Carnall et al. 2019a; Tacchella et al. 2022); thus, properties measured from SED-only fits will always suffer from systematic uncertainties e.g., flux calibrations and different physical models obtained from stellar templates that vary with uncertainties on the data.

To robustly recover and analyze the timescales of a galaxy's stellar mass growth, we need to decipher spectral signatures containing strong imprints of stellar evolution. Continuum spectroscopy in the rest-frame optical regime contains information about the nature of past star formation (bursty, uniform, rising, declining, etc.) and metal enrichment within a galaxy in features like G4300, Fe4383, Fe4531, Mg2, Balmer lines, and the 4000 Å break. These signatures evolve most rapidly in young stellar populations, since more massive galaxies today are generally older by several gigayears, studies of their SFHs should be more accurate and precise at earlier times. To obtain better signal-to-noise ratios (S/Ns), many analyses of high-redshift galaxy surveys involve mass-matched stacking of spectra, losing any information about any individual galaxy's evolution (Schiavon et al. 2006; Choi et al. 2014; Siudek et al. 2017; Cullen et al. 2019). High-S/N continuum spectroscopic data when combined with deep broadband photometric data has the potential to produce much stronger constraints on the SFHs of galaxies (Gallazzi et al. 2008; Pacifici et al. 2012; Thomas et al. 2017; Carnall et al. 2019b; Iyer 2019; Webb et al. 2020; Tacchella et al. 2022) and provide clues on the number of major star formation episodes and the timescales of rejuvenation, starbursts, and quiescence. Spectroscopy alone also suffers from systematics such as instrumental noise and outlier pixels and emphasizes the importance of spectrophotometric modeling.

It is worth noting that even spectrophotometric modeling can be insufficiently sensitive to more slowly evolving old stellar populations, and more so at later epochs. However, it has been argued that photometry can only probe the last ∼1 Gyr of an SFH, whereas adding spectroscopic data can help to probe the SFH further back in time (Chaves-Montero & Hearin 2020). Many studies have been conducted to recover the SFHs of local galaxies (Thomas et al. 2005; Cid Fernandes 2007; Panter et al. 2007; Tojeiro et al. 2009; McDermid et al. 2015; Citro et al. 2016; Ibarra-Medel et al. 2016). However, this approach of using fossil records at $z = 0$ may not lead to reliable results, especially for more massive galaxies for which the major episode of their star formation happened very early in the Universe and these galaxies are now left with predominantly old stellar populations that suffer from strong outshining effects. This underscores the importance of deep spectroscopic studies with high S/N at large lookback times.

Recent advances in computational and sampling techniques (Skilling 2006; Feroz & Hobson 2008; Feroz & Skilling 2013; Feroz et al. 2019) have led to the development of a variety of tools that provide fast full-Bayesian fitting of models to spectrophotometric data, like MCSED (Bowman et al. 2020), BEAGLE (Chevallard & Charlot 2016), `Prospector` (Johnson & Leja 2017; Johnson et al. 2021), and `Bagpipes` (Bayesian Analysis of Galaxies for Physical Inference and Parameter EStimation; Carnall et al. 2018). These Bayesian methods give a better handle on the priors assumed and are robust to the classical problem of overfitting the data with complex models, e.g., (Leja et al. 2019). However, different SSP libraries and modeling assumptions in these tools can influence the derived SFHs (Martins 2021; Pacifici et al. 2023).

Though real SFHs of galaxies are complex, a simplified way to model them is by parameterizing the SFHs using a functional form. The most commonly used forms are exponentially declining (Mortlock et al. 2017; Wu et al. 2018a; McLure et al. 2018), delayed exponentially declining (Ciesla et al. 2017; Chevallard et al. 2019), log-normal (Gladders et al. 2013; Abramson et al. 2015; Diemer et al. 2017; Cohn 2018), and double power law (Ciesla et al. 2017; Carnall et al. 2018). These analytic prescriptions have been shown to match well with many SFHs from simulations (Simha et al. 2014; Diemer et al. 2017) and are widely used as they minimize computational requirements. Increasing complexity by adding bursts of star formation can bring parametric SFHs even closer to realistic scenarios. However, capturing events such as rejuvenation and sudden quenching can still be challenging for parametric models. A more flexible method is nonparametric SFHs—which adopts a series of periods of constant star formation in fixed or flexible time bins (Cid Fernandes et al. 2005; Ocvirk et al. 2006; Cappellari 2017; Iyer & Gawiser 2017; Leja et al. 2017; Chauke et al. 2018). Nonparametric approaches have higher flexibility with a wider range of possible solutions and therefore can allow a broader range of priors on SFHs and decrease biases on recovered results with more realistic episodes of star formation in predefined time bins (Iyer & Gawiser 2017; Leja et al. 2019; Suess et al. 2022a, 2022b).

Until recently, SPS modeling of statistically representative populations has been limited to the analysis of photometry-only data sets. Numerous efforts have been put toward recovering the SFHs of both star-forming and quiescent populations from deep broadband photometric surveys spanning wide redshift ranges (Dye 2008; Wuyts et al. 2009; Pforr et al. 2012; Pacifici et al. 2016a, 2016b; Iyer & Gawiser 2017; Iyer 2019; Aufort et al. 2020; Olsen et al. 2021), due to greater data availability and lower computational demands. In contrast, fewer studies have tested modeling spectrophotometric data for high-redshift galaxies (Carnall et al. 2019b; Estrada-Carpenter et al. 2020; Forrest et al. 2020; Johnson et al. 2021; Khullar et al. 2022; Tacchella et al. 2022; Hamadouche et al. 2023), owing to the dearth of high S/N continuum spectroscopy at significant lookback times. Large spectroscopic surveys like DEEP2 (Newman et al. 2013), MOSDEF (Kriek et al. 2015), and KBSS (Rudie et al. 2012; Steidel et al. 2014; Strom et al. 2017) have been primarily sufficient to characterize emission-line properties of thousands of star-forming galaxies. On the other hand, smaller spectroscopic studies of hundreds of quiescent galaxies have provided windows into the stellar populations of quiescent systems out to $z \sim 2$, but with a significant bias toward the brightest, most massive subset.

The Large Early Galaxy Astrophysics Census (LEGA-C; van der Wel et al. 2016; Straatman et al. 2018; van der Wel et al. 2021) provides a novel opportunity to characterize the full population of Milky Way mass and larger progenitors at a significant lookback time. This deep spectroscopic survey of ∼3000 star-forming and quiescent galaxies looking 6–8 billion yr back in time ($0.6 < z < 1$) includes deep imaging available for each galaxy from the UltraVISTA survey (Muzzin et al. 2013). At this redshift, most stars in LEGA-C survey galaxies are <3 billion yr in age, enabling more robust characterization of their SFHs.

The primary goal of this paper is to measure the SFHs of the full LEGA-C DR3 sample by applying two commonly used Bayesian SPS modeling techniques (with modeling choices optimized for each) on spectrophotometric data and investigate the evolution of massive galaxies before $z \sim 0.8$. We quantify these SFHs in two widely used metrics, namely, t_{50} and t_{90}, corresponding to the times when a galaxy formed 50% and 90% of its total stellar mass, respectively, and study the population trends of these formation times with stellar mass and stellar velocity dispersion.

The structure of the paper is as follows. Section 2 describes the LEGA-C data set and our approach to spectrophotometric modeling using `Bagpipes` and `Prospector`, and some example demonstrations of modeling results. Section 3 describes the SFHs of star-forming and quiescent galaxies and of the full population as recovered from spectrophotometric fits. We show cumulative median mass growth trends in stellar mass bins and further quantify the population trends of t_{50} and t_{90} with stellar mass and stellar velocity dispersion. In Section 4, we expand on the interpretation of our results with respect to previous low- and high-redshift studies and how this impacts our understanding of the formation of both star formation and quiescent systems. In Section 5, we conclude our study and highlight some major takeaways from this analysis. We also speculate on potential future works that could be successors of this study to help us better constrain the evolution of massive galaxies and answer broader questions. Throughout this paper, we assume $\Omega_M = 0.3$, $\Omega_\Lambda = 0.7$, $H_0 = 70$ km s^{-1} Mpc^{-1}, and all magnitudes are quoted in the AB system.

2. Data and Modeling Methods

2.1. Data and Sample

LEGA-C (van der Wel et al. 2016; Straatman et al. 2018; van der Wel et al. 2021) is a 130 night public spectroscopic survey of ∼3000 *Ks*-band selected galaxies targeting redshift range $0.6 < z < 1.0$ in the COSMOS field, looking 6–8 billion yr back in time. Each spectrum has an approximate observed spectral coverage of 6300–8800 Å corresponding to a 3600–5200 Å rest-frame optical regime. The survey was conducted on the Very Large Telescope (VLT) using ViMOS (Le Fevre et al. 2000) and completed its third and final data release (DR3) in 2021 August (van der Wel et al. 2021).

The full spectroscopic sample consists of 4081 galaxies—3029 primary targets and 1052 fillers. Targets were *Ks*-band selected from the UltraVISTA catalog (Muzzin et al. 2013) to include massive galaxies above $\sim 10^{10} M_\odot$ and to have *Ks*-band magnitudes brighter than a redshift dependent limit of [20.7–7.5 log((1+z)/1.8)]. This selection criterion is independent of any derived quantities from the spectra. The full primary sample can be reweighted using sampling and volume corrections following van der Wel et al. (2021) to be mass representative above $\log(M_*/M_\odot) > 10.5$, which we adopt as the mass threshold for this study. Each galaxy was observed for ∼20 hr yielding an S/N ≈ 20 Å^{-1} continuum with high-fidelity absorption and emission-line features for both dusty, blue as well as faint, red galaxies.

As the LEGA-C survey targets only a subset of the full photometric sample, we account for missing galaxies with appropriate weighting to individual galaxies to ensure spectroscopic completeness above the previously specified magnitude limit in a full census of the properties of massive galaxies at that epoch. Hence, throughout this paper, we apply a multiplicative factor $\mathtt{T}_{\mathtt{cor}}$—corresponding to volume and sample correction—from the DR3 catalog (van der Wel et al. 2021) to individual object counts to make it representative of that redshift. The photometric information is taken from UltraVISTA catalog (Muzzin et al. 2013). We use the *BvrizYJ* bands for our primary spectrophotometric analysis.

The stellar mass ($\log(M_*/M_\odot)$), spectroscopic redshift (z), S/N, and integrated stellar velocity dispersion (σ_*) density distributions for the primary sample are shown in Figure 1. All values are taken from the LEGA-C DR3 catalog with (total) stellar mass estimates from `Prospector` photometry-only stellar populations fits (LOGM_MEDIAN), spectroscopic redshift from the LEGA-C spectra (Z_SPEC), the median S/N per pixel of the LEGA-C spectrum (S/N), and stellar velocity dispersion (SIGMA_STARS) estimated from Gaussian broadening of theoretical single stellar population models as described in Bezanson et al. (2018). We split the sample into star-forming and quiescent populations using the Muzzin et al. (2013c) rest-frame *U*–*V* and *V*–*J* color–color cuts, identifying quiescent galaxies with $U\text{–}V > (V\text{–}J) \times 0.88 + 0.69$. Note that throughout this study, we adopt the LEGA-C DR3 catalog value of σ_* and $M_*/M_\odot$ to maintain a single set of labels for each galaxy and to facilitate consistent comparisons with other studies. There are 1774 star-forming (medians: $\log(M_*/M_\odot) \sim 10.8$ and $\sigma_* \sim 140$ km s^{-1}) and 1231 quiescent galaxies (median: $\log(M_*/M_\odot) \sim 11.2$, $\sigma_* \sim 200$ km s^{-1}) in the primary sample of 3005 objects shown in red and blue colors, respectively (obtained using PRIMARY flag in LEGA-C DR3 catalog, more details can be found in van der Wel et al. 2021). Throughout this paper, we focus on objects above the approximate mass completeness limit of the LEGA-C survey ($10.5 < \log(M_*/M_\odot) \leqslant 12$ and $100 < \sigma_* \leqslant 300$ km s^{-1}). For the mass-limited sample, we have an effective sample size of 2703 unique galaxies (1459 star forming and 1244 quiescent) and the velocity-dispersion sample includes 2823 unique galaxies (1575 star forming and 1248 quiescent). This sample selection is shown with dashed and solid lines in Figure 1.

2.2. Spectrophotometric Modeling

In this work, we use two state-of-the-art Bayesian SPS modeling tools, `Bagpipes` (Carnall et al. 2018) and `Prospector` (Johnson & Leja 2017; Johnson et al. 2021),

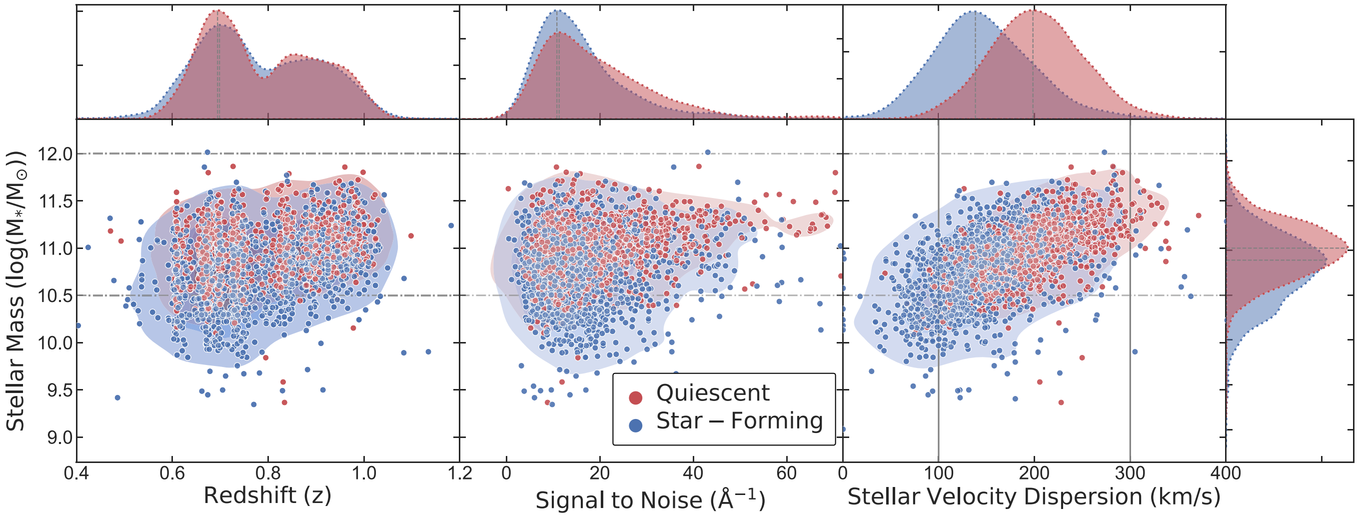

Figure 1. Stellar mass vs. redshift (left), median S/N of LEGA-C spectra (center) and stellar velocity dispersion (right) for all 3005 primary LEGA-C galaxies from the DR3 catalog with density distributions of star-forming (blue) and quiescent (red) populations based on rest-frame *UVJ* colors. Our effective sample selections are shown with dashed–dotted lines (mass selected) and solid lines (velocity dispersion selected).

to perform a full spectrophotometric fitting of the primary LEGA-C galaxies. Details of the two methods used in this work are discussed in Sections 2.2.1 and 2.2.2. We use the *BvrizYJ* bands in our primary spectrophotometric analysis following the conclusions in Appendix B in van der Wel et al. (2021). That study finds that using photometry longward of a rest frame of $\sim$0.8 μm disagrees with popular SPS models and leads to systematic errors in fits to the SED of $\sim$20% of their sample, which in turn propagated into the stellar mass, star formation rate (SFR), dust attenuation, and other population parameters. We check the robustness of our results by performing comparisons with two more parametric sets of fits altering the photometric data: (1) spectra +*vriz* bands and (2) spectra + 20 bands (*B* to 24 μm, namely, *B, g, IA484, IA527, V, IA624, r, IA679, IA738, i, z, y, J, H, Ks, ch1, ch2, ch3, ch4, mips24)* covering 15 Subaru bands (*B–Ks*), four IRAC bands (*ch1–ch4*), and one Spitzer MIPS24 band, ranging from UV to far-IR wavelengths. The results of this comparison are shown in Figure A1 in the Appendix.

2.2.1. Bagpipes

`Bagpipes` is an SPS modeling package built on the updated BC03 (Bruzual & Charlot 2003) spectral library[15] with the 2016 version of the MILES library of empirical spectra that includes 2.5 Å resolution in the 3525–7500 Å wavelength range (Falcón-Barroso et al. 2011). It is built on a Kroupa (2001) initial mass function (IMF) assumption and utilizes the `MultiNest` nested sampling algorithm (Feroz et al. 2019) to produce posterior distributions of physical parameters. We perform parametric full spectral SPS modeling of LEGA-C spectra with *BvrizYJ* UltraVISTA broadband photometry using a double power-law SFH (Ciesla et al. 2017; Carnall et al. 2018), parameterized as

$$\mathrm{SFH}(t) \propto \left[\left(\frac{t}{\tau}\right)^{\alpha} + \left(\frac{t}{\tau}\right)^{-\beta}\right]^{-1}. \tag{1}$$

This model has three free parameters describing the rising (β), falling (α), and peak (τ) of star formation, whereas other widely used options (e.g., exponential, delayed tau, and log-normal) have two or fewer free parameters. Hence, by construction, the double power-law SFH has more flexibility. Tau models are shown to fail to recover mock SFHs (Carnall et al. 2019a) and simulation SFHs (Pacifici et al. 2012). A double power-law SFH is chosen, owing to its ability to recover the redshift evolution of cosmic SFRD (Behroozi et al. 2013; Gladders et al. 2013; Madau & Dickinson 2014) and owing to the agreement with simulation results (Pacifici et al. 2016b; Diemer et al. 2017). The rising and falling slopes essentially do not change beyond the prior ranges chosen (becoming either flat or vertical), owing to the analytical functional form (Equation 1) and cover full variations of possible SFHs within this limit. The stellar metallicity is assumed to be the same for all stars born. This value is linearly interpolated on a grid of SSP models and is allowed as a free parameter varying from (0.02, 2.5)$Z_\odot$ uniformly in linear space. The $Z_\odot$ value is assumed to be 0.02 in BC03 models. We test the impact of choosing linear and logarithmic priors on the stellar metallicity on the derived posterior values in our spectrophotometric fits for a subset of galaxies and find no strong deviations. The last free SFH parameter is the stellar mass formed in the entire lifetime of a galaxy until the point of observation (without mass return to the ISM); we allow $\log(M_*/M_\odot)$ to vary logarithmically from (0, 13). Two bursts on top of a double power law are included to account for any abrupt variation in star formation activity. Each burst is given the flexibility of age, stellar mass, and stellar metallicity and hence three free parameters. We use the Charlot & Fall (2000) dust model with two free parameters—*V*-band attenuation and the slope of attenuation. We adopt a second-order spectral calibration and white uncorrelated noise for spectral pixels, for which a detailed description can be found in Carnall et al. (2019b). Dust emission models from Draine & Li (2007) are implemented with fixed $Q_{\mathrm{pah}} = 2$, $U_{\mathrm{min}} = 1$, and $\gamma_e = 0.01$. While testing multiple parameter options and analyzing the full posterior distributions of the output stellar population properties, we found that nebular emission-line modeling in Bagpipes biased the stellar metallicities of star-forming galaxies to high values ($\log(Z_*/Z_\odot) > 0.35$). Additionally, we were concerned that the limiting ionizing radiation of young stars could inappropriately

---

[15] http://www.bruzual.org/bc03/Updated_version_2016/

Table 1
`Bagpipes` Modeling Parameters and Prior Distribution Functions

No.	Property	Parameters	Symbol/Unit	Prior	Range	Remarks
1	SFH	alpha	α	Logarithmic	(0.01,1000)	Falling slope
2	Double power law	beta	β	Logarithmic	(0.01,1000)	Rising slope
3		tau	τ/Gyr	Uniform	(0.1,15)	Peak of star formation
4		Stellar metallicity	$Z_*/Z_\odot$	Uniform	(0.02,2.5)	From grid interpolation
5		Stellar mass	$M_*/M_\odot$	Logarithmic	(0,13)	Priors from Carnall et al. (2019b)
6	Burst-1	Age	Gyr	Uniform	(0,13)	Delta function burst
7		Stellar mass	$M_*/M_\odot$	Logarithmic	(0,10)	With three free parameters
8		Stellar metallicity	$Z_*/Z_\odot$	Uniform	(0,2.5)	
9	Burst-2	Age	Gyr	Uniform	(0,13)	Same as above
10		Stellar mass	$M_*/M_\odot$	Logarithmic	(0,10)	
11		Stellar metallicity	$Z_*/Z_\odot$	Uniform	(0,2.5)	
12	Dust	V-band attenuation	Av/mag	Uniform	(0.,2.0)	Charlot & Fall (2000)
13		Slope of attenuation	n	Gaussian	(0.3,2.5)	$\mu = 0.7$, $\sigma = 0.3$
14	Stellar velocity dispersion	Sigma	$\sigma_\star$/(km s^{-1})	Logarithmic	(40,400)	Free parameter
15	Redshift	z	$z_{\rm spec}$	LEGA-C		Fixed parameter
16	Spectral white noise	Scaling factor	a	Logarithmic	(0.1,10)	Uncorrelated spectroscopic noise
17	Calibration	Zeroth order	c0	Gaussian	(0.9,1.1)	$\mu = 1$, $\sigma = 0.05$
18	Calibration	First order	c1	Gaussian	(−0.5,0.5)	$\mu = 0$, $\sigma = 0.1$
19	Calibration	Second order	c2	Gaussian	(−0.5,0.5)	$\mu = 0$, $\sigma = 0.1$

Table 2
`Bagpipe` Spectrophotometric Modeling Results

ID	Mask	LEGAC_ID	$z_{\rm spec}$	$\sigma_{*,\rm cat}$ (km s^{-1})	$\log(M_{*,\rm cat}/M_\odot)$	$\log(M_{*,\rm fit}/M_\odot)$	SFR ($M_\odot$ yr^{-1})	t_{50} (Gyr)	t_{90} (Gyr)
103041	17	1159	0.82	75.9	10.52	$10.63\pm^{0.1}_{0.07}$	$5.91\pm^{2.02}_{1.14}$	$5.07\pm^{0.24}_{0.18}$	$6.01\pm^{0.13}_{0.14}$
103061	16	1160	0.72	193.1	11.03	$11.25\pm^{0.03}_{0.03}$	$0.00\pm^{0.00}_{0.00}$	$3.54\pm^{0.24}_{0.03}$	$5.72\pm^{0.03}_{0.06}$
103155	19	1161	0.64	103.1	11.07	$11.36\pm^{0.07}_{0.06}$	$17.26\pm^{3.67}_{2.54}$	$2.79\pm^{0.03}_{0.03}$	$6.29\pm^{0.00}_{0.01}$
103179	16	1162	0.62	108.1	10.75	$11.02\pm^{0.04}_{0.04}$	$0.00\pm^{0.00}_{0.00}$	$3.22\pm^{0.41}_{0.29}$	$5.18\pm^{0.20}_{0.15}$
103274	14	1163	0.92	175.9	11.06	$11.43\pm^{0.04}_{0.04}$	$6.12\pm^{0.74}_{0.47}$	$1.02\pm^{0.30}_{0.12}$	$3.56\pm^{0.52}_{0.26}$

Note.
[a] We display a sample table for formatting; the full data table is available to download online.

(This table is available in its entirety in machine-readable form.)

describe emission lines produced by either evolved stars or active galactic nuclei (AGNs) (and bias the SFR estimates), especially in such a diverse and massive sample of galaxies (Carnall et al. 2019b). Thus, we choose to mask the emission lines from the fit. Stellar velocity dispersion is another free parameter modeled with a variable Gaussian kernel in velocity space. Although the DR3 LEGA-C spectra used in this study are flux calibrated using the UltraVISTA photometry (van der Wel et al. 2021), we include an additional polynomial function of wavelength to address any higher-order spectrophotometric calibration uncertainties. We use a second-order Chebyshev polynomial function with Gaussian priors—zeroth order centered around unity and first and second orders centered around zero (see Section 4.3.1 in Carnall et al. 2019b for more details). This modeling requires an average of ∼70 CPU hr per galaxy. A further description of all modeling parameters and prior distributions is shown in Table 1. Modeling results are included in Table 2. We notice a subset (total 126 in the full sample/4.2% of the full population) of the quiescent population that prefers very similar best-fitting SFHs with ages $t_{\rm mw} \sim 3$ Gyr and $3.160 < t_{\rm lw} < 3.163$. We investigated these objects and found them well constrained in parameter space, spanning a range of empirical properties such as spectral indices, *UV–VJ* colors, and redshifts.

2.2.2. Prospector

`Prospector` is a Bayesian SPS modeling tool that allows nonparametric modeling of the SFH of a galaxy in piecewise constant SFR time bins. (Johnson et al. 2021). It deploys the Flexible Stellar Population Synthesis (FSPS) package with the MILES stellar library and MIST isochrones to model stellar properties (Conroy et al. 2009). We use a Chabrier (2003) IMF and the Kriek & Conroy (2013) dust law with nebular continuum and line emissions modeled with CLOUDY (Ferland et al. 2013). Note that this choice differs from the `Bagpipes` modeling; we found that modeling nebular emission with Cloudy grids within `Prospector` produced well-behaved posterior distributions. We also tested the impact of including/excluding physical modeling of emission lines in Prospector on a subset of a total of 300 galaxies (150 quiescent and 150 star forming) with significantly detected emission lines and high S/N spectra (O II EW > 4 and S/N > 12). In general,

Table 3
`Prospector` Modeling Parameters and Prior Distribution Functions

No	Parameter	Description	Prior
1	σ_*	Velocity dispersion	Fixed to LEGA-C values
2	$\log(M/M_\odot)$	Total stellar mass formed	Uniform in log space: min = 7, max = 12
3	$\log(Z/Z_\odot)$	Stellar metallicity	Uniform in log space: min = −1.98, max = 0.4
4	SFR ratios	Ratios of adjacent SFRs	Student's t-distribution ($\sigma = 0.3$, $\nu = 2$)
5	$z_{\rm spec}$	Redshift	Prior: LEGA-C spectroscopic redshift ±0.005
6	$\hat{\tau}_{\lambda,2}$	Diffuse dust optical depth	Clipped normal: min = 0, max = 4, mean = 0.3, $\sigma = 1$
7	$\hat{\tau}_{\lambda,1}$	Birth cloud dust optical depth	Clipped normal in ($\hat{\tau}_{\lambda,1}/\hat{\tau}_{\lambda,2}$): min = 0, max = 4, mean = 0.3, $\sigma = 1$
8	n	Kriek & Conroy (2013) dust-law slope	Uniform: min = −1, max = 0.4
9	$\log(Z_{\rm gas}/Z_\odot)$	Gas-phase metallicity	Uniform: min = −2, max = 0.5
10	$\log U$	Ionization parameter	Uniform: min = −4, max = −1
11	$\sigma_{\rm eline}$	Emission-line amplitude	Uniform: min = 30, max = 300
12	ν	Spectral white noise	Uniform: min = 1, max = 3
13	cp	Photometric calibration	Uniform: min = 10^{-5}, max = 0.5
14	cs	Spectroscopic calibration	Uniform: min = 10^{-5}, max = 0.5

the recovered SFHs agree for each galaxy within uncertainties. In a small subset of quiescent galaxies ($N = 11$), nonphysical modeling of the emission lines results in maximally old stellar populations that are formed in dramatic, but uncertain, bursts of star formation in the earliest time bin. Given the overall agreement between the two sets of models and slightly more extended SFHs in the aforementioned subset, we include the physical line ratio modeling in our `Prospector` fitting. We use the z-nested sampling option (Speagle 2020) for posterior sampling, similar to `Bagpipes`. This nonparametric approach is capable of recovering complex SFHs and capturing abrupt star formation processes such as sudden quenching and rejuvenation events. On the other hand, fitting both the galaxy spectra and SED is highly computationally expensive and requires about ∼100 CPU hr per galaxy to fit an eight fixed bin SFH model with 14 free parameters.

In this work, we adopt a continuity prior piecewise constant SFH with the Student's t-distribution that fits the change in log (SFR(t)) in adjacent time bins, while weighing against abrupt changes in SFR(t). This prior has also been shown to robustly reproduce mock and more importantly, simulated SFHs (Lower et al. 2020). The pioneering work of Ocvirk et al. (2006) shows that a maximum of eight episodes of SFH can be independently recovered from an optical spectra of resolution of $R = 10{,}000$, $S/N = 100$, and wavelength coverage of $\lambda = 4000$–6800 Å, with the distinguishability of simple stellar populations proportional to the separation in logarithmic time. Hence we use an eight time bin SFH model (five logarithmically spaced) in our analysis. The eight bins of constant SFRs are distributed as follows (in lookback time):

$$
\begin{gathered}
0 < t < 30\text{Myr} \\
30\text{ Myr} < t < 100\text{ Myr} \\
100\text{ Myr} < t_{\log1,2,3,4} < 0.85 t_{\rm univ}\ (5\log\text{ bins}) \\
0.85 t_{\rm univ} < t < t_{\rm univ}.
\end{gathered}
$$

The two most recent fixed bins capture signatures of any recent abrupt star formation, one earliest fixed bin corresponding to the oldest stellar populations spans the first 15% of cosmic time, with five logarithmically spaced bins in between. Redshift is set to the LEGA-C spectroscopic redshift with an allowed ±0.005 variation and stellar velocity dispersion is fixed to the LEGA-C DR3 catalog values. A full description of the free and fixed parameters of the `Prospector` model and their adopted priors are included in Table 3 and modeling results are reported in Table 4.

One might be concerned that priors on the SFHs could drive differences in the inferred SFHs that are derived from the two software packages. We test this by drawing from the prior distributions in each set of models. Figure 2 depicts the prior probability density from `Bagpipes` (orange) and `Prospector` (green) when 1000 random samples are drawn from the SFH parameterization described in Tables 1 and 3 (more details can be found in Sections 2.2.1 and 2.2.2). For ease of comparison, we assign a floor SFR value of 0.001 $M_\odot$ yr^{-1} to arbitrarily small SFR values. The median distributions of prior SFHs are shown in solid lines, whereas the 16th and 84th percentiles are shown with dotted lines. The median values follow closely for both the codes, except at the earliest times the analytic function requires SFR($t = 0$) = 0, whereas nonparametric models assign nonzero star formation in the earliest bin. This figure suggests no strong biases in SFRs with lookback times from the priors adopted in the two codes.

As shown in this section, we find the expected differences in the SFHs for individual galaxies as derived by the two modeling methods. We explore the impact of these choices on the full population of massive galaxies in the remainder of the paper.

2.3. Modeling Results and Examples

First, we emphasize that all SFHs are allowed to start from the Big Bang; however, the analytic SFHs (`Bagpipes`) naturally exhibit more flexibility in onset time (with negligible star formation in early times for some cases) and slope than the early bins in piecewise constant nonparametric SFHs (`Prospector`). Although in principle the first bin in the latter models could exhibit negligible star formation, the fits prefer at least some nonzero average SFR at the earliest times. Also, since bins represent SFRs averaged over an extended period of

Table 4
`Prospector` Spectrophotometric Modeling Results

ID	Mask	LEGAC_ID	$z_{\rm spec}$	$\sigma_{*,\rm cat}$ (km $\rm s^{-1}$)	$\log(M_{*,\rm cat}/M_\odot)$	$\log(M_{*,\rm fit}/M_\odot)$	SFR ($M_\odot$ $\rm yr^{-1}$)	t_{50} (Gyr)	t_{90} (Gyr)
103041	17	1159	0.82	75.9	10.52	$10.64\pm^{0.05}_{0.06}$	$1.27\pm^{8.80}_{0.47}$	$3.72\pm^{0.11}_{0.09}$	$5.94\pm^{0.03}_{0.43}$
103061	16	1160	0.72	193.1	11.03	$11.37\pm^{0.02}_{0.02}$	$0.15\pm^{2.50}_{0.12}$	$2.40\pm^{0.01}_{0.01}$	$4.66\pm^{0.36}_{0.19}$
103155	19	1161	0.64	103.1	11.07	$11.19\pm^{0.03}_{0.02}$	$14.34\pm^{15.61}_{2.01}$	$4.32\pm^{0.52}_{0.66}$	$6.70\pm^{0.34}_{0.02}$
103179	16	1162	0.62	108.1	10.75	$11.04\pm^{0.02}_{0.02}$	$0.19\pm^{2.05}_{0.13}$	$2.60\pm^{0.11}_{0.17}$	$5.27\pm^{0.27}_{0.26}$
103274	14	1163	0.92	175.9	11.06	$11.35\pm^{0.04}_{0.04}$	$3.82\pm^{7.41}_{1.80}$	$2.36\pm^{0.01}_{0.11}$	$4.83\pm^{0.04}_{0.36}$

Note.
[a] We display a sample table for formatting; the full data table is available to download online.

(This table is available in its entirety in machine-readable form.)

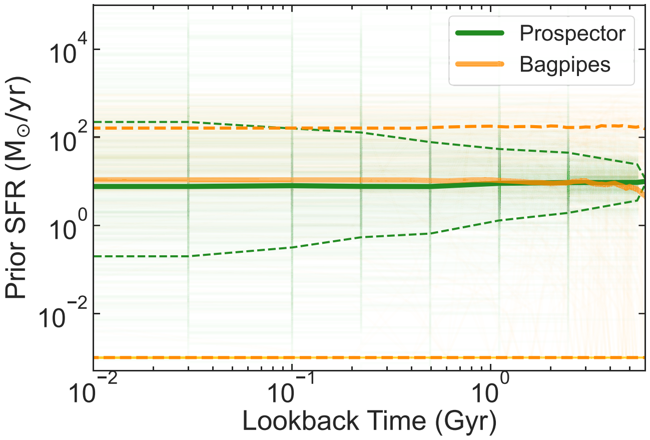

Figure 2. Prior density distribution of SFH obtained by drawing 1000 samples from the parameterization described in Table 1 (`Bagpipes`) and Table 3 (`Prospector`). Thick lines show the medians (solid) and dashed 1σ (16th–84th percentile) scatter. The median values closely follow those in both codes, except at the earliest times, the analytic function requires $\mathrm{SFR}(t=0)=0$ and nonparametric models assign nonzero star formation in the earliest bin.

time, they are more likely to be nonzero. This discrepancy is partially driven by differences in modeling choices and also likely reflects a lack of constraining power in the data at the earliest times, even with the high S/N of the LEGA-C data set. Fundamentally such information is in the prior-dominated regime; in this paper, we quantify the ultimate impact of popular choices on aggregate SFHs of the populations.

Figures 3 and 4 show representative examples of spectrophotometric modeling and recovered SFHs of four quiescent and four star-forming galaxies, respectively. In the left column, each panel shows an observed LEGA-C spectrum and UltraVISTA photometry (gray), along with the best-fitting models from `Bagpipes` (orange) and `Prospector` (green). The insets show the full *BvrizYJ* photometric SEDs and models. We note that the models fit both the spectroscopic and photometric data very well. The residuals are quantified in χ values in the bottom panel ($\chi=$ (observed flux–model flux)/error). Gray bands indicate regions that are masked to avoid emission lines in the `Bagpipes` modeling. The right large panels show the corresponding SFHs. Note that we chose to logarithmically scale the lookback time (horizontal axis) to highlight the most robustly measured epochs at late times.

For quiescent galaxies (Figure 3), we note that both models provide excellent fits to the observed data and median SFHs agree reasonably well, more so in late times than early times, when quantified in the formation time metrics t_{10}, t_{50} and t_{90} ($\Delta t_{10}|_{\rm median}=2.05$ Gyr, $\Delta t_{50}|_{\rm median}=1.47$ Gyr, and $\Delta t_{90}|_{\rm median}=0.22$ Gyr with uncertainties (calculated from posteriors) of order of 0.27/0.13/0.20 Gyr in each delta metric, respectively. Note that these are representative of the full LEGA-C quiescent population statistics ($\Delta t_{10}|_{\rm median}=2.41$ Gyr, $\Delta t_{50}|_{\rm median}=1.38$ Gyr, and $\Delta t_{90}|_{\rm median}=0.23$ Gyr). One subtle difference emerges at the earliest times when `Prospector` consistently assigns finite star formation in the first time bin leading to older stellar populations, whereas this is not necessarily the case for parametric SFHs in `Bagpipes`. For star-forming galaxies (Figure 4), we see better agreement in median SFRs at later times compared to the quiescent examples above, with differences in timescales within the uncertainties. ($\Delta t_{10}|_{\rm median}=0.49$ Gyr, $\Delta t_{50}|_{\rm median}=0.28$ Gyr, and $\Delta t_{90}|_{\rm median}=0.14$ Gyr with uncertainties of the order of 1.25/0.84/0.22 Gyr in each delta metric, respectively). Note that these are representative of the full LEGA-C star-forming population statistics ($\Delta t_{10}|_{\rm median}=1.30$ Gyr, $\Delta t_{50}|_{\rm median}=0.34$ Gyr, and $\Delta t_{90}|_{\rm median}=0.17$ Gyr). Further mass and sigma trends of the full LEGA-C sample will be analyzed in the following sections.

3. Star Formation Histories of Massive Galaxies

In this section, we combine the median SFHs derived for each galaxy in the LEGA-C sample to characterize the overall growth histories of massive galaxies. We first interpolate all SFHs on a uniform age grid from (0.01, 8) Gyr and impose a minimum SFR (floor) of 0.001 $M_\odot$ $\rm yr^{-1}$ to arbitrarily small SFR values. For each galaxy, we take the median SFH from the posterior distributions and combine these medians to calculate population medians in bins of (1) stellar mass and (2) stellar velocity dispersions from the LEGA-C DR3 catalog. For ease of presentation, we first focus on three coarse stellar mass bins representative of the LEGA-C primary sample: (a) $10.5<\log(M_*/M_\odot)<11$, (b) $11<\log(M_*/M_\odot)<11.5$, and (c) $11.5<\log(M_*/M_\odot)<12$, and four coarse stellar velocity dispersion bins: (a) $100<\sigma_*\,(\rm km\,s^{-1})<150$, (b) $150<\sigma_*\,(\rm km\,s^{-1})<200$, (c) $200<\sigma_*\,(\rm km\,s^{-1})<250$, and (d) $250<\sigma_*\,(\rm km\,s^{-1})<300$, and later increase the resolution to finer bins to characterize population trends. Note that the mass and sigma values used to bin galaxies are taken from the LEGA-C DR3 catalog (LOGM_MEDIAN, SIGMA_STARS) and are mass-loss corrected, as described in detail in Section 2. These catalog values have mean offsets of +0.05 dex and −0.02 dex with `Bagpipes` and `Prospector` modeling results, respectively. In each mass/velocity dispersion bin, each SFH is weighted by $T_{\rm cor}$ (which includes both a volume and

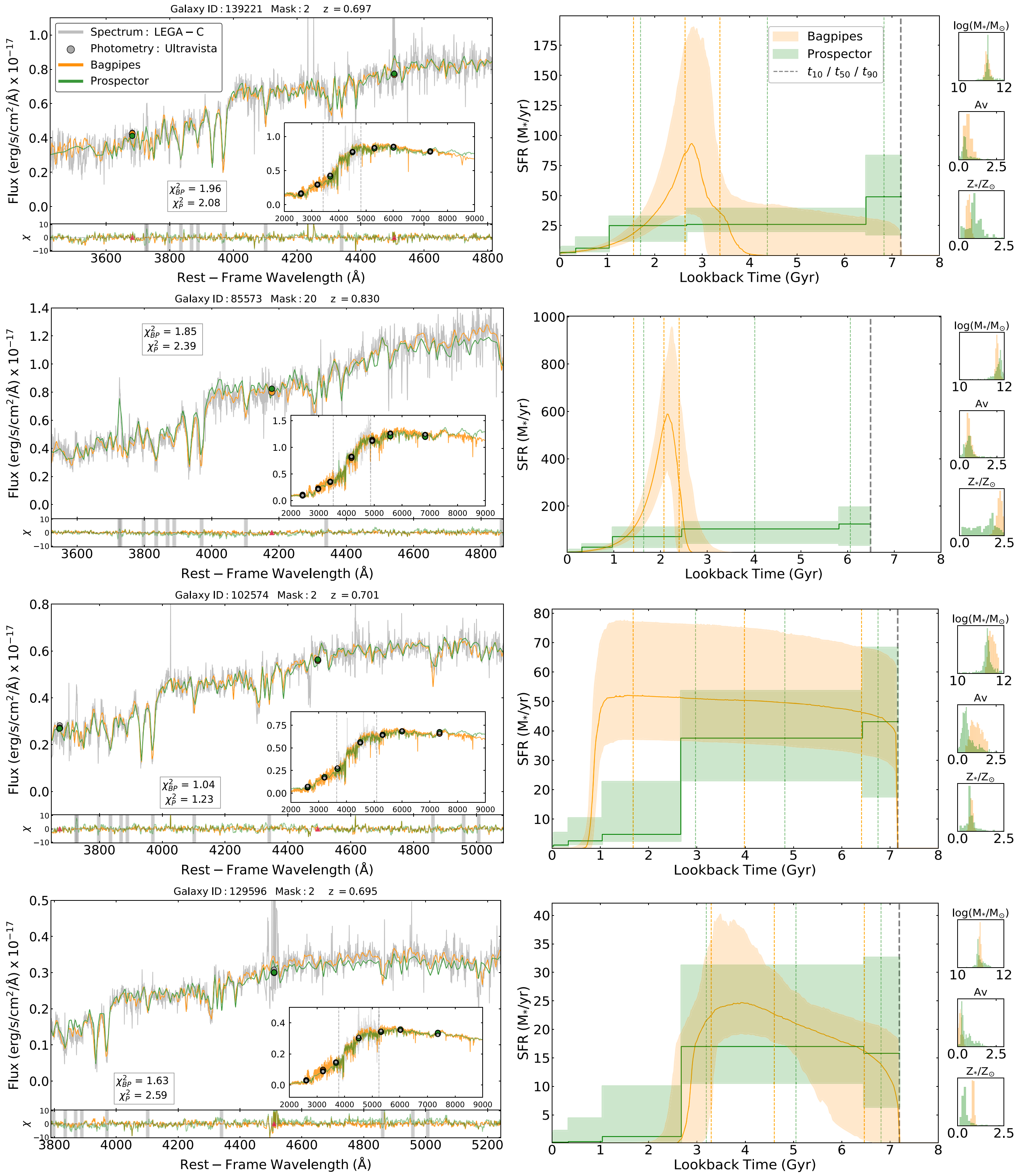

Figure 3. Spectrophotometric modeling (left) of four representative quiescent galaxies using LEGA-C spectra and UltraVISTA photometry (gray) along with best-fit models from `Bagpipes` (orange) and `Prospector` (green). The lower sub-panels show χ values (data-model/error) with gray bands showing regions masked in parametric modeling. Reduced chi-squared values are quoted in inset boxes. The right panels show median SFHs (solid lines) and 16th–84th percentile distributions of the posteriors (shaded regions). The vertical dashed lines from left to right correspond to 90%, 50%, and 10% formation timestamps for each tool (color coded accordingly). The right-most column shows the posterior distributions of stellar mass (without mass loss), dust Av, and stellar metallicity. Both modeling techniques yield good fits to the data, and overall, the SFHs agree reasonably well in late times (t_{90}), with some divergence at early times (t_{10}).

sample correction factor, for details see van der Wel et al. (2021) Appendix A) in the calculations of population median and scatter to account for the LEGA-C survey targeting strategy.

To demonstrate our approach to combining the posteriors from individual fits, we show the individual median and population trends in an example subset of LEGA-C data in Figure 5. The top row shows individual median SFHs from the

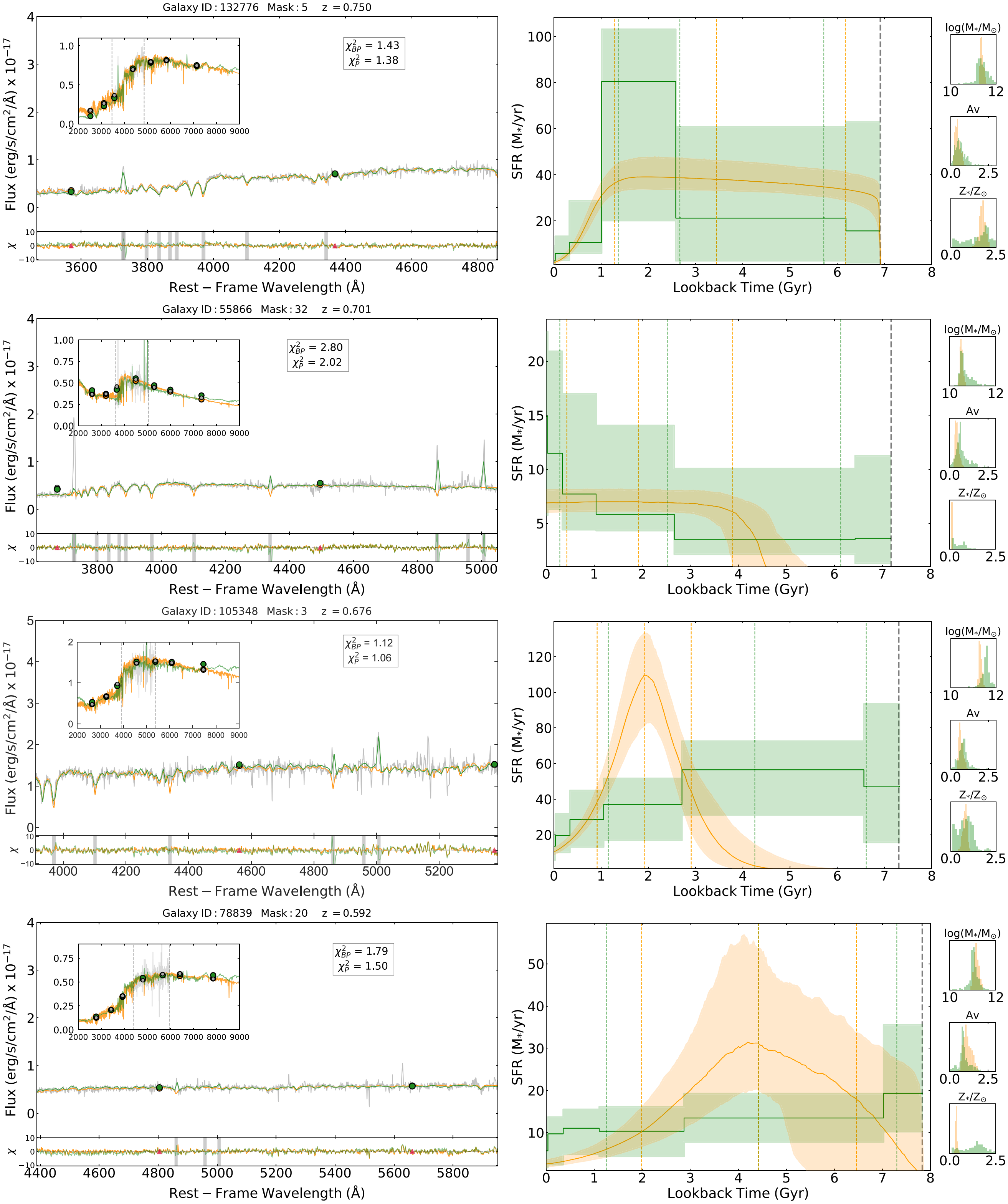

Figure 4. Four representative star-forming galaxies with modeling outputs in the same format as described in Figure 3. In general, parametric and nonparametric SFHs for individual star-forming galaxies agree reasonably well at all times.

two methods for the most massive quiescent galaxies in the stellar mass bin of $11.5 < \log(M_*/M_\odot) < 12$. `Bagpipes` SFHs are shown in orange and `Prospector` SFHs are shown in green. The middle and right panels show these SFHs in specific star formation rate (log(sSFR)) as a function of time. sSFR at an epoch is obtained by dividing SFR at that epoch by the total stellar mass formed up until that epoch, excluding mass loss. The center panel includes median SFHs for individual galaxies and the right panel collapses these to show only the population distributions. The bottom row shows these

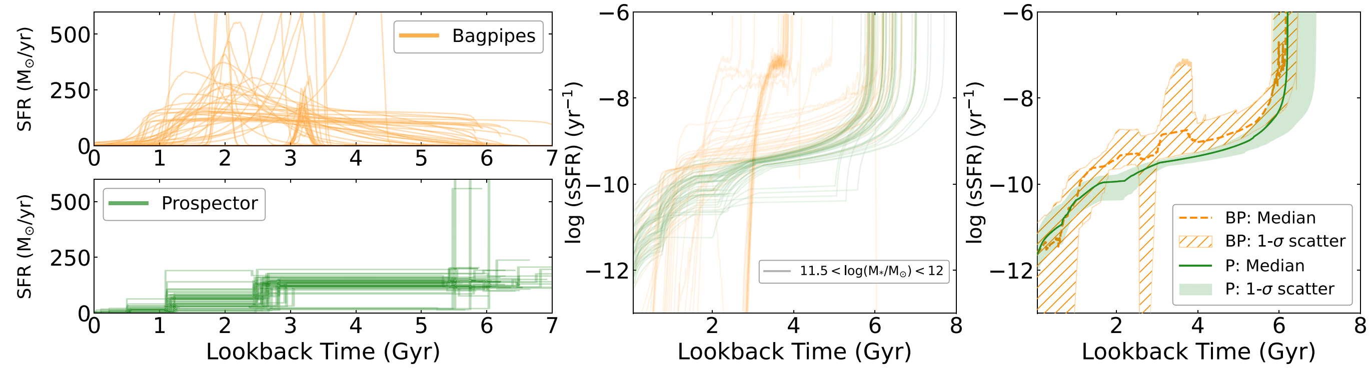

(a) Quiescent

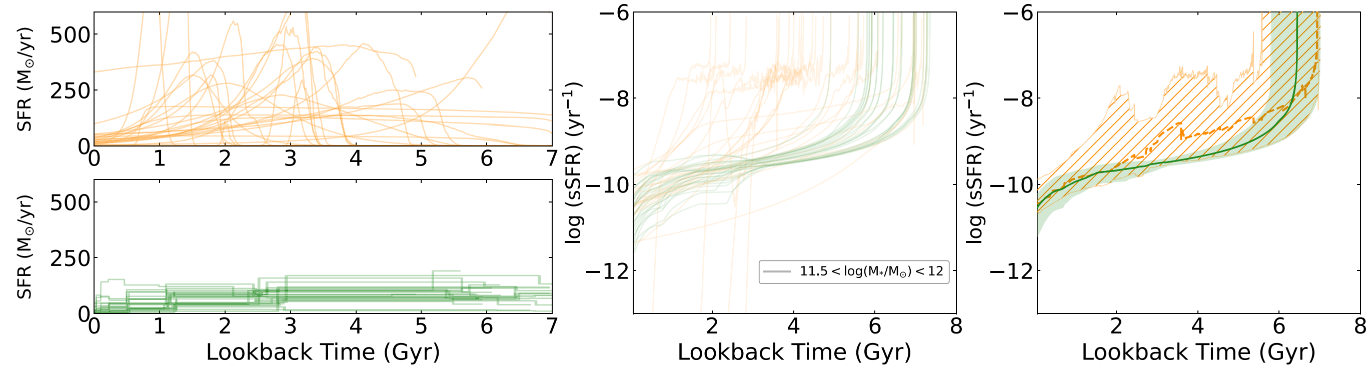

(b) Star-forming

Figure 5. Individual (left) and population (center and right) SFHs recovered from `Bagpipes` and `Prospector` for two example samples of massive ($11.5 < \log(M_*/M_\odot) < 12$) quiescent galaxies (top row (a)) and star-forming galaxies (bottom row (b)). The middle panel shows individual SFHs in the sSFR and the right panel shows the 16th, 50th, and 84th percentile population distributions. Note that `Bagpipes` generates relatively higher population scatter due to variation in the onset and truncation of the double power-law parameterization, in contrast with the early onset of star formation inferred from nonparametric models.

trends for the most massive star-forming population. Note that `Bagpipes` has more variety in onset, duration, and quenching of star formation for individual galaxies, which are often imprinted on the population trends even though the individual parametric SFHs are smooth. In addition to the 126 galaxies with questionable fits that are discussed in Section 2, there is a significant number of quiescent galaxies in `Bagpipes` with t_{50} formation times between 3 and 4 Gyr, as evident in the SFHs in Figure 5 (similarly for other mass bins, see Figure A2 in the Appendix).

Figure 6 expands on the right panel in Figure 5 to show the sSFR evolution in three stellar mass bins (rows) for star-forming galaxies (left), quiescent galaxies (center), and the full population (right). Each panel shows the population medians (dashed lines/solid lines) and the 16th–84th percentile population scatter (hashed/filled regions) for `Bagpipes` and `Prospector`, respectively. The bottom row combines the median trends of all mass bins with thin shaded regions showing 1σ error on the medians calculated from bootstrapping. We adopt the transition and quiescence boundaries as $(1/3\ t_{\rm H})$ and $(1/20\ t_{\rm H})$ from Tacchella et al. (2022), where $t_{\rm H}$ is the Hubble time at $z_{\rm median} = 0.8$. Although individual galaxies show a variety of SFHs, the population median trends are largely independent of stellar mass, with slight trends at early times that are dominated by the demographics of the LEGA-C sample and modeling priors. In part, differences in the onset of star formation can be partially due to slight differences in the mass-dependent redshift distributions of the LEGA-C sample. However, as discussed in Section 2, the modeling priors also introduce subtle differences. `Bagpipes` consistently measures slightly higher median sSFRs, especially within the quiescent population and shows higher population scatter compared to Prospector. Median sSFR trends within the star-forming population show better agreement between the two codes. To quantify this, for each mass bin, we calculate the median of the differences between the curves. In Figure 6, from top to bottom—median $\Delta s{\rm SFR}(t)|_{\rm SF} = 0.08$, 0.12, and 0.31 yr^{-1} (left column), median $\Delta s{\rm SFR}(t)|_{Q} = 0.22$, 0.25, and 0.29 yr^{-1} (middle column), and median $\Delta s{\rm SFR}(t)|_{\rm ALL} = 0.11$, 0.18, and 0.30 yr^{-1} (right column). For star-forming galaxies, both codes infer that massive galaxies fall to lower sSFRs at the point of observation than the less massive ones. Some differences are seen in the median trends of the most massive galaxies (red) from the two codes that could be attributed to the small sample size. For quiescent galaxies, we see a large diversity of `Bagpipes` sSFR tracks. We do not find that the population of massive quiescent galaxies shut off before lower-mass counterparts. Note that this is different from local Universe findings (Nelan et al. 2005; Gallazzi et al. 2006).

Figure 7 focuses on the median trends in the cumulative stellar mass growth and adopts the same plotting conventions as used in Figure 6, except the horizontal axis now shows the age of the Universe, starting at the Big Bang. The hashed and filled regions show the 16th–84th percentile distributions of individual median SFHs from `Bagpipes` and `Prospector`, respectively. Horizontal gray dotted lines correspond to the 10%, 50%, and 90% formation thresholds. These timescales,

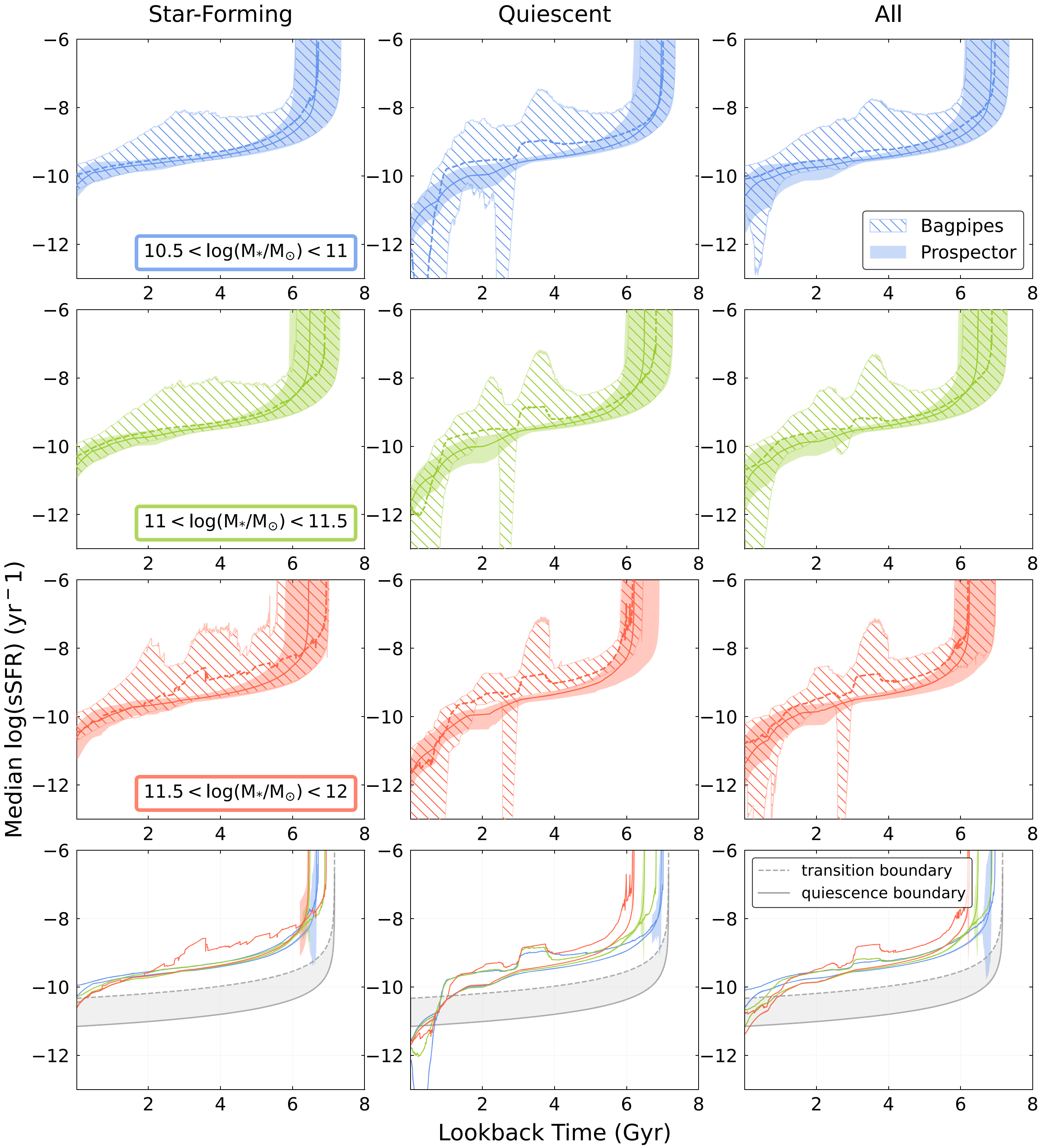

Figure 6. Median sSFRs (log(sSFR)) with lookback time for populations of star-forming (left), quiescent (center), and all (right) galaxies sorted in bins of their stellar mass. Colors indicate stellar mass bins—blue < green < red in increasing mass. `Bagpipes`/ `Prospector` results are shown in dotted lines/solid lines with hashed/shaded regions representing the 16th–84th percentile population scatter. The bottom-most row shows median trends of all mass bins with thin shaded regions representing standard error on the medians via bootstrapping. The transition region from star-forming to quiescence is shown in the gray band. The star-forming population shows overall better agreement between the two methods than the quiescent population. Note that `Bagpipes` has more bursty pathways to reach quiescence.

which we hereby define as t_{10}, t_{50}, and t_{90}, are widely used metrics to quantify the timescales of stellar mass growth in a galaxy, including all progenitors up to the point of observation (Weisz et al. 2008, 2011; Pacifici et al. 2016a; Behroozi et al. 2019). These values are quantified for the full primary sample in Tables 3 and 4. As we find in the previous two figures, parametric models in general show higher population scatter than nonparametric ones due to galaxy-to-galaxy variations. The bottom row compiles all median trends to compare the rate of stellar mass growth across different masses. This cumulative

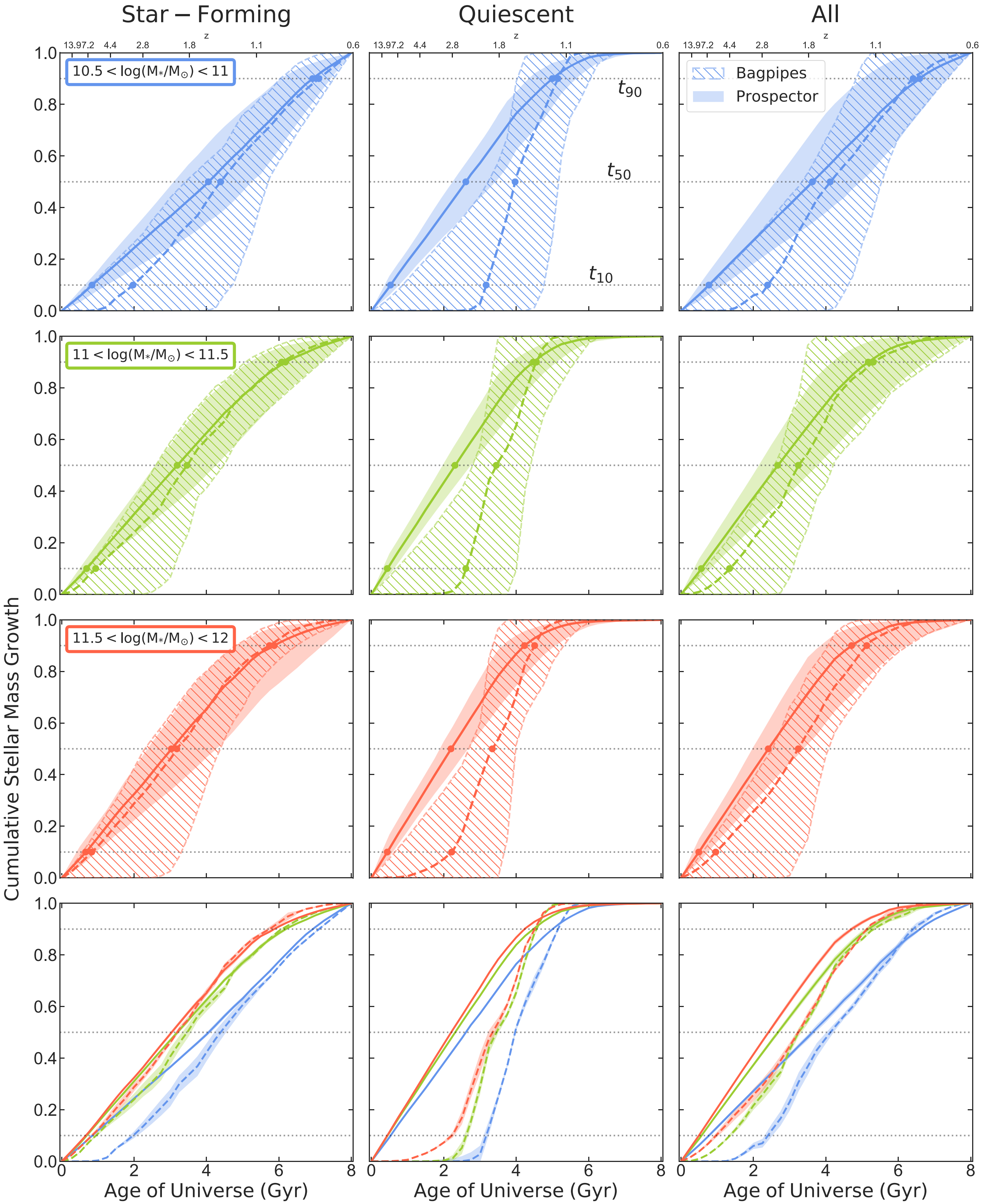

Figure 7. The cumulative stellar mass fractions vs. time for star-forming (left), quiescent (center), and all (right) galaxies sorted by stellar mass. The color and plotting scheme is the same as in Figure 4. This represents a complete census as individual galaxies are weighted by correction factors to reflect the LEGA-C targeting. Lower-mass galaxies grow more slowly than their massive counterparts. Nonparametric SFHs (Prospector, solid) start earlier and are more extended, especially for quiescent galaxies.

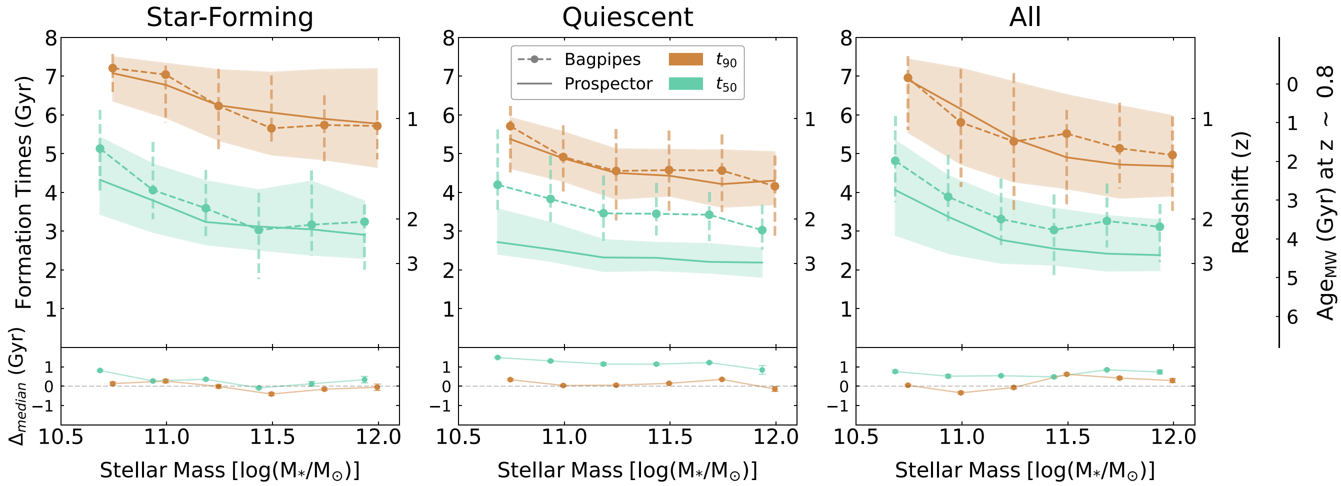

Figure 8. t_{90} (brown) and t_{50} (teal) formation times/redshifts of star-forming, quiescent, and total galaxy populations vs. stellar mass. Error bars/shaded regions indicate the 16th–84th percentile population scatter. The bottom row represents the difference in median values of the Bagpipes and Prospector formation times. The far right panel shows the vertical axis in equivalent mass-weighted ages. As the redshift of individual galaxies is different, this is a first-order age estimate assuming all galaxies are observed at median LEGA-C redshift of $z \sim 0.8$. Late formation times (t_{90}) are consistent between models, with greater disagreement at earlier times (t_{50}), especially for quiescent galaxies. The strong mass trends within the full population (right panel) are primarily driven by star-forming galaxies that dominate the low-mass end.

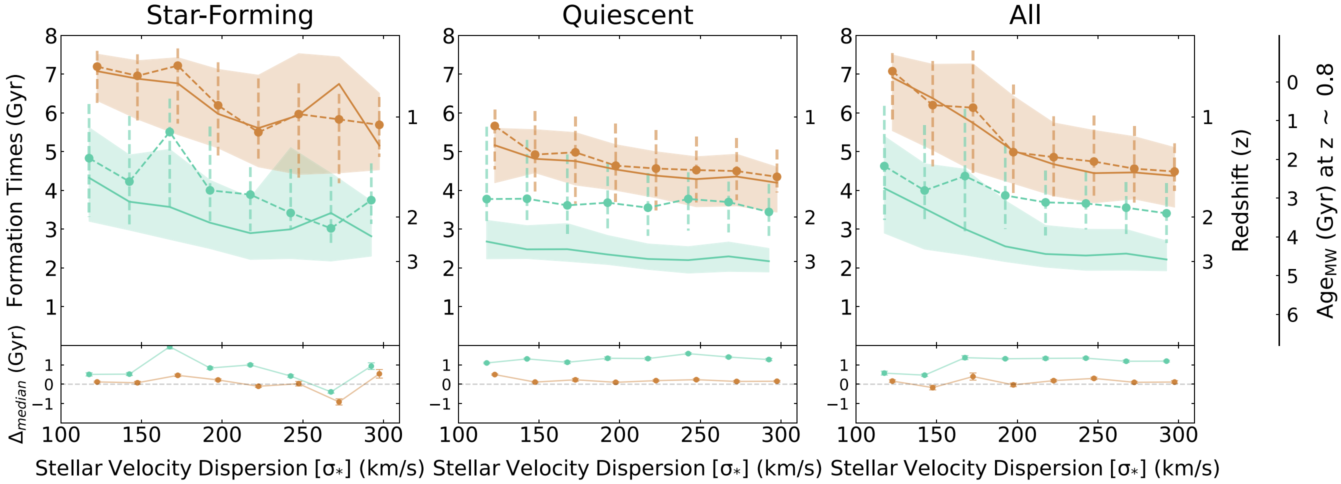

Figure 9. Similar to Figure 8, now binned in stellar velocity dispersion. We find a striking correlation between the formation timescales and stellar velocity dispersion in the full population (right). This trend is in part driven by demographics; the quiescent fraction depends more strongly on stellar velocity dispersion than stellar mass (e.g., Taylor et al. 2022).

view highlights both mass trends within the populations and discrepancies at early times, due to modeling degeneracies and prior assumptions. At any given time, low-mass galaxies have grown less than massive galaxies. Significant discrepancies in t_{10}, and to some degree in t_{50}, suggest that SFHs are prior dominated at large lookback times. Perhaps similar deep spectroscopic observations of galaxies at even earlier times (e.g., with JWST) will help to break modeling degeneracies and resolve this issue, but at this epoch, the measurements of the earliest SFHs of massive galaxies will remain prior dominated, even with high S/N spectroscopic data.

Figures 8 and 9 show t_{50} (teal) and t_{90} (brown) the formation timescales for the populations of star-forming (left), quiescent (center), and all galaxies (right) versus stellar mass and stellar velocity dispersion, respectively. We exclude t_{10} because of the dramatic disagreement between the two sets of models at early times, suggesting that its measurements are completely prior dominated. `Bagpipes`' median trends and population scatter are shown with dotted lines and error bars and `Prospector's` as solid lines with shaded bands. The bottom row shows the difference between the median values derived from the two methods with (very small) error bars indicating the standard error in the medians. The measured late formation times (t_{90}) agree well across all stellar masses, with a slight offset in early formation times (t_{50}), especially of quiescent systems (t_{50}, $\Delta_{\mathrm{median,SF}} < 0.9$ Gyr, $\Delta_{\mathrm{median,Q}} < 1.8$ Gyr, $\Delta_{\mathrm{median,ALL}} < 0.9$ Gyr, and t_{90}, $\Delta_{\mathrm{median,SF}} < 0.4$ Gyr, $\Delta_{\mathrm{median,Q}} < 0.3$ Gyr, and $\Delta_{\mathrm{median,ALL}} < 0.6$ Gyr). This consistent offset in t_{50} for quiescent systems could be partially driven by the preference for a more flexible onset of star formation in `Bagpipes` compared to `Prospector`. We find clear trends in both t_{50} and t_{90} with stellar mass among star-forming galaxies. In contrast, the median formation times are mostly independent of mass among the quiescent galaxies. The overall correlation with mass is reflected by the full population, in which the younger star-forming galaxies dominate at low masses and are rare at the massive end. We note that similar correlations with stellar mass remain within finer redshift bins ($\Delta z = 0.1$). Correlations of formation times

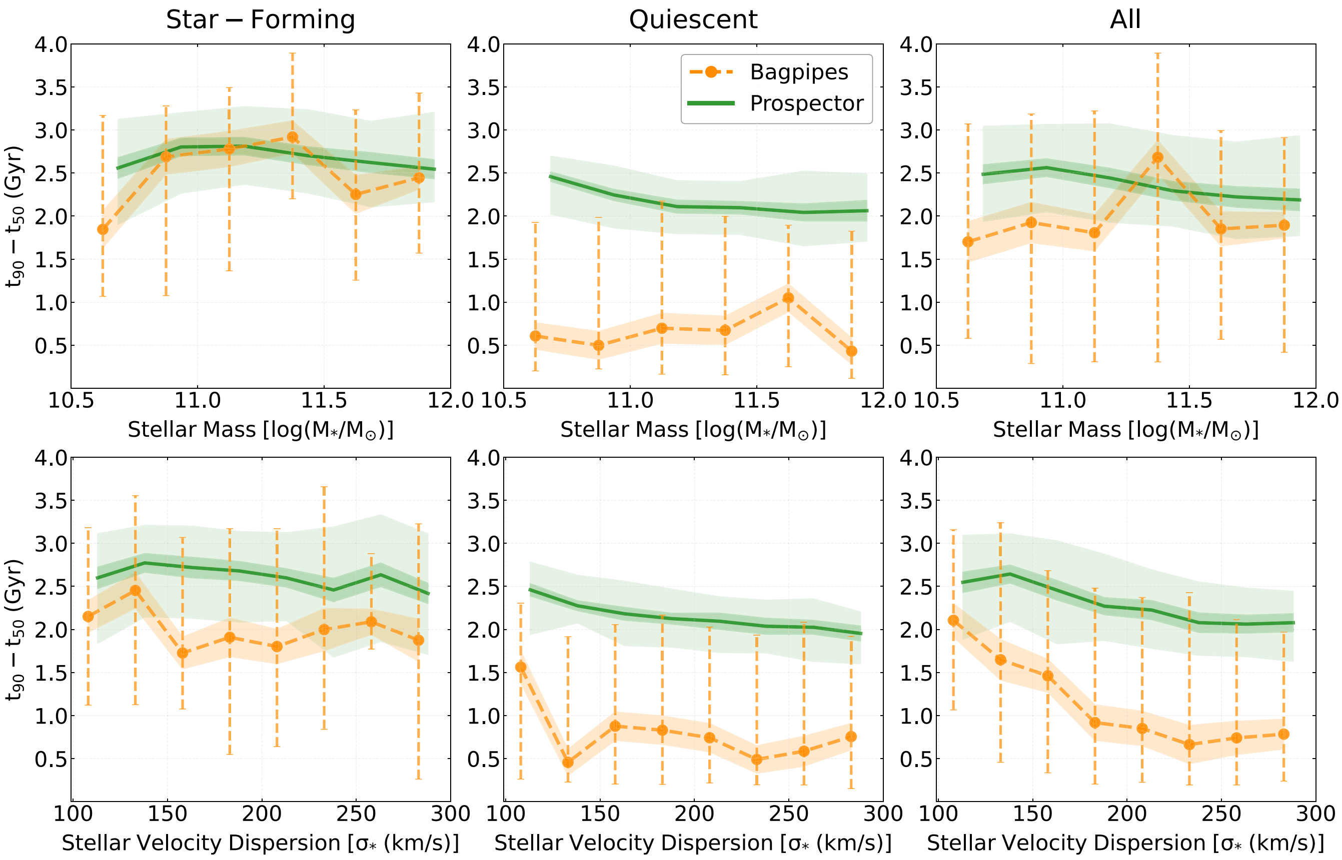

Figure 10. The distribution of duration of star formation at late times ($\tau_{\mathrm{SF,late}} \equiv t_{90} - t_{50}$) in stellar mass (top row) and stellar velocity dispersion (bottom row) bins for the population of star-forming (left), quiescent (center) and all (right) as recovered from `Bagpipes` and `Prospector`. Green solid lines and orange solid points represent the 50th percentile values (median) and broad green-shaded regions and orange error bars represent the 16th–84th percentile population scatter in that bin. The standard error on the medians is represented in slightly darker thin shaded regions calculated from bootstrapping. Nonparametric models are consistently more extended than the double power-law SFHs. We find no strong correlation between $\tau_{\mathrm{SF,late}}$ and stellar mass or stellar velocity dispersion. This lack of correlation is in contrast with trends found among analogous massive elliptical galaxies today (e.g., Graves et al. 2009; Greene et al. 2022). The significant offset between the $\tau_{\mathrm{SF,late}}$ of star-forming and quiescent galaxies does imprint a trend in the full population median value with stellar velocity dispersion (bottom row, right-most panel), where demographics are more cleanly separated than in stellar mass.

with stellar velocity dispersion are qualitatively similar to those with stellar mass (Figure 9). Again, the median t_{50} and t_{90} formation times are essentially uniform for the quiescent population. However, because the fraction of star-forming galaxies plummets at high stellar velocity dispersion (especially above $\sigma_\star \gtrsim 200$ km s^{-1}) (Taylor et al. 2022), the formation timescales of the full population exhibit an even stronger correlation with stellar velocity dispersion (Figure 9, right panel).

Finally, we investigate the duration of late-time star formation (t_{90}–t_{50}) from `Prospector` (green) and `Bagpipes` (orange) in Figure 10. Some studies have used (t_{80}–t_{20}) and (t_{90}–t_{10}) timescales (Pacifici et al. 2016a; Tacchella et al. 2022) to quantify the full duration of star formation, but we choose to avoid large uncertainties at earlier times and quantify late-time star formation as $\tau_{\mathrm{SF,late}} \equiv t_{90}$–$t_{50}$. Figure 10 shows these timescales versus stellar mass (top row) and stellar velocity dispersion (bottom row) with error bars/shaded regions representing the population scatter, following the plotting conventions of Figures 8 and 9. Here we see that while agreement is reasonably good between, e.g., median t_{50} in the two models, systematic offsets in the duration of star formation remain. Nonparametric models from `Prospector` exhibit consistently more extended SFHs than those derived with double power-law models. This discrepancy at the earliest times has been well documented (e.g., Carnall et al. 2019a; Leja et al. 2019). Notably, the median $\tau_{\mathrm{SF,late}}$ from `Bagpipes` is dramatically (∼2 Gyr) more rapid for quiescent galaxies, with an enormous population scatter, reflecting the larger variety of SFHs (see, e.g., Figure 5). Mock recovery testing of $\tau_{\mathrm{SF,late}}$ using spectrophotometric data could reveal if this timescale is recoverable. Leja et al. (2019) and Carnall et al. (2019b) have shown that with mock photometric data, `Prospector` was able to recover late-time star formation better than `Bagpipes`. Note that the low $\tau_{\mathrm{SF,late}}$ values in `Bagpipes` are partially driven by flexibility in onset times as well as in the late-time SFH parameter (e.g., falling slope alpha) to adapt steep/shallow values to give a range of t_{90}–t_{50} values. In fact, the population scatter on `Bagpipes` star-formation duration detracts from the informative nature of the median trends. However, a significant offset between the $\tau_{\mathrm{SF,late}}$ of star-forming and quiescent galaxies does imprint a trend in the full population median value with stellar velocity dispersion (bottom row, right-most panel), where demographics are more cleanly separated than in stellar mass (e.g., Franx et al. 2008; Belli et al. 2014; Taylor et al. 2022, Figure 9). The median duration of star formation derived by `Prospector` does not vary significantly within the star-forming population, but quiescent galaxies exhibit a slight decrease with stellar mass and stellar velocity dispersion ($\lesssim$0.5 Gyr across the full range). This is consistent with weak correlations between alpha enhancement and stellar velocity dispersion for a subset of quiescent galaxies from the same LEGA-C data set (Beverage et al. 2023).

4. Discussion

Star-formation activity has been demonstrated to depend both on stellar mass (Kauffmann et al. 2004; Pacifici et al. 2016a; Calvi et al. 2018) and on stellar velocity dispersion (Franx et al. 2008). It has been long debated whether stellar velocity dispersion is a more fundamental property than stellar mass (Wake et al. 2012; Zahid et al. 2018; Sharma et al. 2021), as it is directly connected to the total gravitational potential well (including the effects of dark matter halo and the supermassive black hole at the galactic center) in which a galaxy resides (Dutton et al. 2010; Elahi et al. 2018).

This census of SFHs builds on extensive studies based on a complete photometric (e.g., Dye 2008; Pacifici et al. 2016a, 2016b; Iyer & Gawiser 2017; Iyer 2019; Aufort et al. 2020; Olsen et al. 2021) and smaller and/or less complete, and more observationally expensive, spectroscopic data set (e.g., Gallazzi et al. 2008; Sánchez-Blázquez et al. 2011; Carnall et al. 2019b, 2022; Tacchella et al. 2022). For the first time at a significant lookback time, we present a comprehensive view of the SFHs of the full population of massive galaxies (not just quiescent or star-forming galaxies separately). This builds on a preliminary study by Chauke et al. (2018) based on early LEGA-C data (607 galaxies) with simpler modeling assumptions: adopting fixed solar metallicity and piecewise constant SFRs using composite stellar population templates from the FSPS package (Conroy et al. 2009). This current paper expands in both scope and detail to yield a comprehensive analysis of the full LEGA-C sample.

Our results are in qualitative agreement with previous analyses, and quantitative differences can generally be attributed to modeling systematics. Previous studies have found similar correlations between formation times t_{50} and stellar mass and stellar velocity dispersion, e.g., for $10.5 < \log(M_*/M_\odot) < 12$, the linear relation goes from (forward in time) 1.8–0.9 Gyr for the quiescent sample in Tacchella et al. (2022), 1.9–1.4 Gyr for the quiescent sample and 3–2.5 Gyr for the star-forming sample in Ferreras et al. (2019), ~1 Gyr for the quiescent sample and ~4–2 Gyr for the star-forming sample across the full mass range in Chauke et al. (2018), which is similar to what we find in our analysis shown in Figures 8 and 9. Interestingly, both of our modeling methods recover significant population scatter in the late-time formation timescales of star-forming galaxies; however, the median $\tau_{\rm SF,late}$ is almost independent of stellar mass. This result is in contrast with previous studies. One interesting comparison is with the work in Estrada-Carpenter et al. (2020), in which $\tau_{\rm SF,late}$ is defined as the quenching timescale (t_Q). Using `Prospector` to fit nonparametric SFHs to a much smaller sample of ~30 quiescent systems at $0.7 < z < 1$, finding a median formation redshift $z50$ roughly corresponding to 3.3–1.5 Gyr formation times for $10.5 < \log(M_*/M_\odot) < 12$, which is consistent within our measured population scatter (Figure 8, `Bagpipes` 4.2–3.0 Gyr; `Prospector` 2.8–2.3 Gyr). However, they find a broader range of quenching timescales varying from 0.4 to 2.2 Gyr, which is different from our $\tau_{\rm SF,late}$ derived using `Prospector` (Figure 10, 1.7–2.7 Gyr) but similar to what we find in `Bagpipes` (Figure 10, 0.2–2.3 Gyr). We can only speculate that this subtle difference could be driven by priors, sample size, or differences in data characteristics (e.g., the use of low-resolution grism spectra). Beverage et al. (2023) studied 135 LEGA-C massive quiescent galaxies based on elemental abundance patterns and found a slightly stronger correlation between formation times and stellar velocity dispersion. The highest dispersion galaxies (>250 km s^{-1}) formed the earliest around 3.1 Gyr and are the most metal-rich, whereas low-dispersion galaxies (<150 km s^{-1}) formed around 4.4 Gyr. This is qualitatively similar to our findings shown in Figure 9, middle panel.

Interestingly, although the qualitative trends agree well with cluster galaxies at a similar epoch, there may be some hint of environmental effects on SFHs. Khullar et al. (2022) find t_{50} of massive quiescent cluster galaxies to be inversely correlated with stellar mass at $0.3 < z < 1.4$ with values within 2 Gyr. This is ~1 Gyr/2 Gyr earlier than our `Prospector`/`Bagpipes` estimates. Again, this difference could be driven by modeling systematics (e.g., that study adopts a delayed tau SFH) or a physical manifestation of environmental processes that combine to quench galaxies earlier or generally speed up galaxy evolution in clusters. Even within the LEGA-C data set age-sensitive indices (Dn4000 and Hδ) of quiescent galaxies depend on the environment, not just in cluster versus field; galaxies in overdense regions are older and formed earlier than those in less extreme environments (Sobral et al. 2022). We note that direct comparisons between different studies can be challenging; Webb et al. (2020) performed a cluster analysis at similar redshifts and found little difference between the ages of galaxies in the field versus cluster environments at fixed mass.

Next, we investigate whether our results from LEGA-C at $z \sim 0.8$ differ significantly from our understanding of this time period as recovered from previous modeling of their presumed descendent galaxies in the local Universe. We start by comparing to SPS modeling of local elliptical galaxies from McDermid et al. (2015). Figure 11 shows a comparison of the median formation times t_{50} and t_{90} as a function of the virial mass for all galaxies in our sample at $\langle z \rangle = 0.8$ from `Bagpipes` (dashed line) and `Prospector` (solid line) relative to quiescent systems at $z \sim 0$ (diamonds) from McDermid et al. (2015), after subtracting the minimal cumulative stellar mass growth between $z \sim 0$ and $z \sim 0.6$. The error bars and shaded regions represent 1σ dispersion in the population medians. The vertical axis is forward in time with $t = 0$ corresponding to the Big Bang. Note that these elliptical galaxies at $z \sim 0$ could either be quiescent or star forming at our redshift; hence, for a first-order comparison with LEGA-C, we compare to the full (left) and quiescent only (right) populations. Virial masses have been calibrated for the majority of the LEGA-C sample (van der Wel et al. 2022) using spatially resolved stellar kinematics (van Houdt et al. 2021). For this simplistic calculation, we adopt a median offset of 0.33 dex between the stellar and dynamical mass for each LEGA-C individual object. McDermid et al. (2015) found that most massive galaxies ($\log(M_*/M_\odot) > 11$) had already accumulated >95% of their stellar mass by $z \sim 0.6$, whereas low-mass galaxies had formed ~90% of their stellar mass. They also found ubiquitously earlier ($t_{50} = 2$ Gyr) stellar mass growth (diamonds with dotted line), than the view from LEGA-C using either modeling framework. This reveals a natural uncertainty of stellar population modeling for the oldest local stellar systems. We see similar dynamical mass trends shown in the left panel for $z \sim 0.8$ galaxies (both star forming and quiescent)

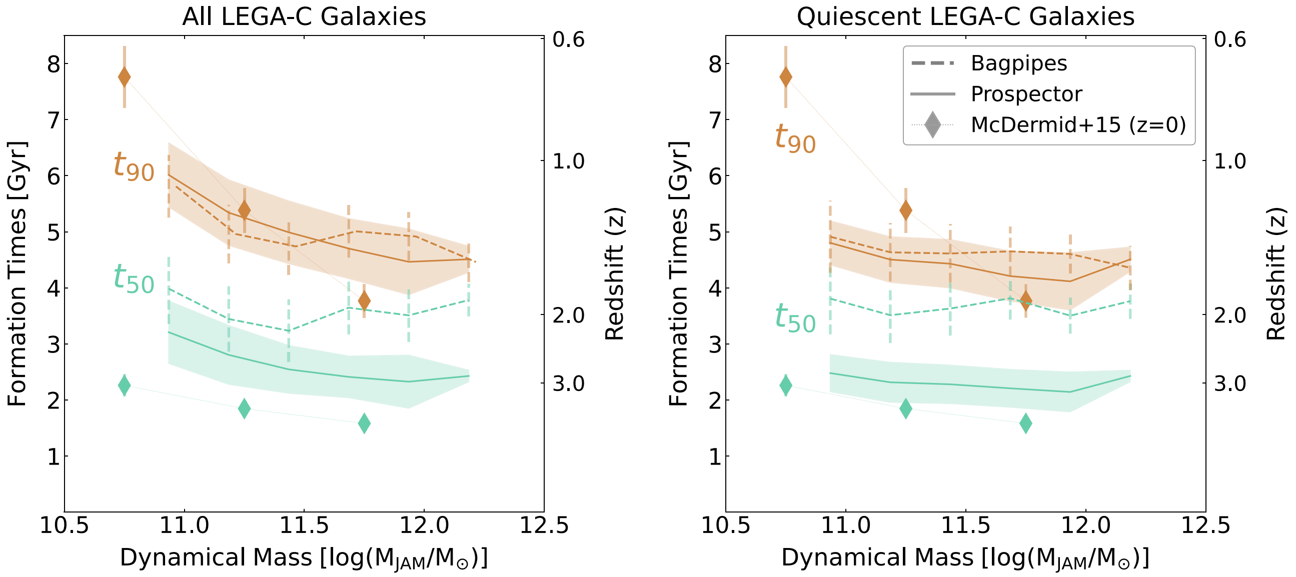

Figure 11. Comparison of median formation times t_{50} (teal) and t_{90} (brown) measured forward in the direction of the age of the Universe in bins of dynamical masses. These are derived for the progenitor populations from the LEGA-C sample and compared to those inferred from local elliptical galaxies from ATLAS3D (after correcting for stellar mass growth between $z \sim 0.8$ and $z \sim 0$) in McDermid et al. (2015). The left panel compares the full LEGA-C population (star-forming and quiescent progenitors) and the right panel compares only quiescent galaxies to the local ellipticals. Error bars and shaded regions represent a 1σ dispersion in the population medians. SPS modeling of local ellipticals finds ubiquitously earlier ($t_{50} \sim 2$ Gyr) star formation (diamonds), which is even more extreme than even nonparametric SFHs for LEGA-C progenitors. The strong trends in later star formation (t_{90}) suggest the importance of star-forming progenitors joining the population at $M_{\rm dyn} \sim 10^{11} M_\odot$ since $z \sim 0.8$.

and local ellipticals, especially toward the low-mass end. This correlation is weaker when only quiescent galaxies from the LEGA-C sample are included. This emphasizes the importance of star-forming progenitors joining the local elliptical population.

Thomas et al. (2005, 2010) provide clear evidence from a $z \sim 0$ sample of galaxies that the duration and timing of galaxy formation depend strongly on the stellar mass, arguing that this ultimately reflects halo assembly. However, even at $z \sim 0.8$, we do not find these trends, even when star-forming progenitors are included. Some of these differences could be attributed to modeling systematics, e.g., the use of a Gaussian SFH prescription to describe population average, chemical enrichment models/abundance patterns, various environmental dependence, and most importantly aperture effects—probing the central few kiloparsecs (not the full galaxy) with a 3″ diameter fiber that makes results more mass dependent for older ages and higher metallicities, whereas slit aperture effects are not that extreme. Furthermore, the view from maximally old galaxies in the local Universe will always be complicated by the relative challenge of modeling slowly evolving old stellar populations. However, it is hard to escape the conclusion that suggests that the trends found in local ellipticals reflect the transformation and assembly/merger history of massive galaxies and not just their in situ SFHs.

Finally, we compare our measured formation time trends for quiescent galaxies with similar studies at other epochs. Figure 12 shows the comparison of median formation times (t_{50}) of massive quiescent systems from our study (orange and green bands indicating population scatter) with other empirical (spectroscopic) studies and simulations across redshifts. The Choi et al. (2014) results (gray solid lines) are derived from full spectral fitting based on alpha abundance measurements and SSP equivalent ages. The gray band indicates the mean formation times recovered from the VANDELS survey ($1 < z < 1.3$) in Carnall et al. (2019b) using `Bagpipes`. The single JWST spectroscopic observation around $z = 4.65$ from Carnall et al. (2023b) is shown with a star symbol. We note that the incredibly small uncertainty on formation time reflects the incredible data quality and limits imposed by the age of the Universe at that early time. Trends found in cosmological simulations at $z = 1$ are shown with dashed (SIMBA, Davé et al. 2019) and dotted (`IllustrisTNG-100`, Nelson et al. 2019) lines. For details on the simulation selection, see Carnall et al. (2019b). Although modeling differences could introduce significant systematic offsets with respect to our fits (e.g., extended SFH versus SSPs, scaled solar metallicity versus alpha enrichment), it is interesting to speculate whether some of the observed offset in t_{50} between epochs is physical, perhaps driven by late additions to the quiescent population. This progenitor bias could exaggerate the evolution of these scaling relations without changing the stellar populations of any individual galaxies. Superficially, the older LEGA-C ages from `Prospector` are roughly consistent with the trend found for quiescent galaxies in VANDELS at higher z; however, our `Bagpipes` modeling adopts much more similar priors and provides a more consistent comparison. Thus, the observed offset between the gray and orange bands suggests that the relation evolves even between $z \sim 1.15$ and $z \sim 0.8$. Choi et al. (2014) modeled stacked optical spectra of massive quiescent galaxies from $0.1 < z < 0.7$ from the Sloan Digital Sky Survey and AGES. Although our spectrophotometric modeling of individual galaxies differs from their analysis, the similar offset to later formation times in lower-redshift quiescent populations is consistent with new additions shifting the scaling relations, perhaps more efficiently at lower mass. There is one caveat in comparing with local elliptical galaxies: galaxy mergers are also major avenues of mass growth and therefore will also contribute to the spatially integrated ages of galaxies (e.g., t_{50} and t_{90}). With SPS

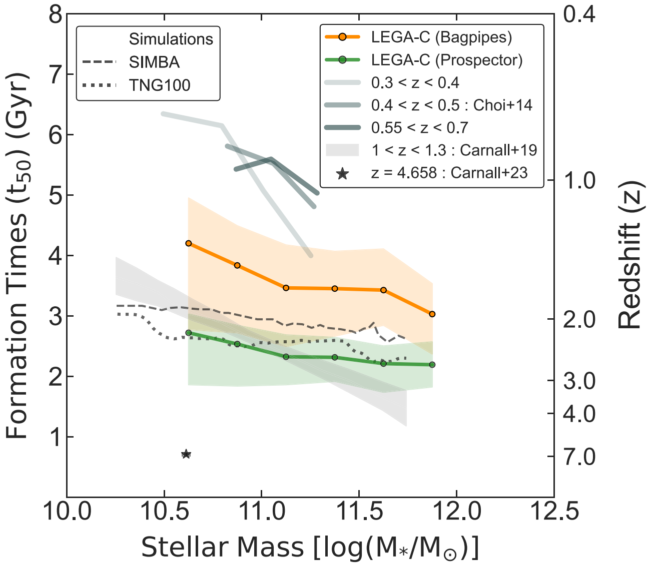

Figure 12. Formation times vs. stellar mass for massive quiescent galaxies across redshifts. The gray lines and bands indicate relations at lower and higher redshifts, respectively (Choi et al. 2014; Carnall et al. 2019b). The highest redshift measurement from JWST is shown with a black star (Carnall et al. 2023a). Our results are shown in orange (parametric SFHs) and green (nonparametric SFHs). Shaded color bands represent the 16th–84th percentile population scatter in the median values. Scaling relations from cosmological simulations (dashed–dotted lines, Davé et al. 2019; Nelson et al. 2019) agree well with our `Prospector` models. The evolution in this relation for quiescent galaxies emphasizes the importance of including star-forming progenitors and ex situ contributions when comparing the stellar populations of galaxies across cosmic time.

modeling, we measure the formation times of stars from all progenitors of a galaxy at $t_{\rm obs}$, which can be quite different from assembly times (t_a). Hill et al. (2017b) demonstrate that this can be a significant effect, by $z\sim0.1$ assembly times and light-weighted formation times can differ by up to ∼2.5 Gyr (see also, e.g., Hill et al. 2017a; Muzzin 2017). We hence note that progenitor-descendant linking is further complicated by the uncertain importance of merging.

Note that one of the key findings of this study is the impact of priors of SPS modeling on early formation time recovery at $z\sim0.8$, even with high S/N data. A part of this is also driven by the outshining of old populations. A natural conclusion, therefore, is that the earliest SFHs can be better understood by modeling the light from galaxies at progressively earlier times, when this becomes less of a concern. Future spectroscopic studies of higher redshifts can precisely pinpoint the emergence of massive quiescent systems and can help settle uncertainties at the earliest times. Recent results from JWST photometry-only SED analyses suggest that massive galaxies may indeed form efficiently and rapidly within 1 Gyr of the Big Bang (e.g., Labbé et al. 2023). However, given uncertainties in the emission-line contributions to photometry (e.g., McKinney et al. 2023), spectroscopic data are needed more than ever. JWST/NIRSpec has been shown to provide the sensitivity required to constrain the SFHs and quenching timescales of galaxies at higher redshifts and lower masses, e.g., Carnall et al. (2023b)'s extreme massive quiescent galaxy at $z=4.65$ included in Figure 12. Other recent studies include those of Looser et al. (2023) and Nanayakkara et al. (2023). Larger, more complete spectroscopic samples from JWST will be crucial to map the early evolution of today's massive quiescent galaxy population. These samples will hopefully shed more light on the modeling degeneracies at the earliest times.

5. Conclusions

In this paper, we analyze the median SFHs of massive ($\log(M_*/M_\odot) > 10.5$) galaxies at $0.6 < z < 1.0$ from the LEGA-C survey by quantifying their formation times (t_{50} and t_{90}) and investigate the population trends in this census with stellar masses and stellar velocity dispersions. From our spectrophotometric analysis, we conclude that:

1. The two modeling methods (parametric and nonparametric) yield consistent late-time SFHs for star-forming and quiescent galaxies. Nonparametric SFHs consistently prefer earlier stellar mass formation, especially for quiescent systems. Potential reasons could be stellar population outshining driving this inference into a systematics-limited regime emphasizing the dominance of modeling priors at the earliest times or a host of different modeling assumptions, e.g., SPS models, treatment of emission lines, dust, parameterization of SFHs, etc. (Figures 2 and 5).
2. Although individual galaxies show a variety of SFH pathways, the median sSFR evolution is similar for all mass bins. Bagpipes' SFHs show population scatter at any time. Both codes infer that massive star-forming galaxies exhibit falling sSFRs with redshift. Neither model finds a mass dependence in the median time at which quiescent galaxies cross an sSFR threshold (Figure 6).
3. From median trends, we find that for both nonparametric and parametric SFH modeling, quiescent galaxies formed 90% of their stars well within an age of ∼4 and ∼5.5 Gyr of the Universe for the massive and less massive ends, respectively. Our analysis reflects the established impact of these priors at earlier times, yielding differences in mass-weighted ages $t_{50}\sim1.5$ Gyr) within that population, with SFHs that further diverge at earlier times. (Figures 7 and 8).
4. Lower-mass galaxies are slightly younger than massive galaxies (Figure 7); however, this trend is relatively weak. This is perhaps due to the fact that the full LEGA-C sample only probes a limited dynamic range in stellar mass. This picture is also consistent with simulations (Shamshiri et al. 2015; Torrey et al. 2018; Iyer et al. 2020). The formation times of star-forming galaxies correlate with stellar mass and stellar velocity dispersion, but similar trends do not exist among the quiescent galaxies. For a combined population, the formation times depend strongly on the M_* and σ_* as the quiescent fraction increases with each property. (Figures 8 and 9).
5. For the star-forming population, both codes recover consistent median formation times ($|t_{\rm Bagpipes}-t_{\rm Prospector}| < 300$ Myr); the most massive systems formed within $t_{50}/t_{90}\sim3$ to 5.5 Gyr and the less massive ones within ∼5 to 7 Gyr (Figure 8, or similarly for high/low $\sigma_\star$, Figure 9). Even for these galaxies, SFRs were on the decline by the time of observation, corroborating a number of previous studies (e.g., Feulner et al. 2005; Ilbert et al. 2015).
6. The late-time duration of star formation ($\tau_{\rm SF,late}=t_{90}-t_{50}$) does not exhibit a significant correlation with $M_\star$ or $\sigma_\star$ for quiescent or star-forming galaxy populations. At face

value, this is in contrast with expectations from the local Universe (e.g., Thomas et al. 2005). We posit that this suggests the importance of transformation, quenching, and/or ex situ evolution even at late times ($z < 1$) (Figure 10).

The remaining open questions include connecting quenching timescales (defined from recovered SFHs), environment, and processes driving quenching in quiescent systems to stellar mass and stellar velocity dispersion. A number of studies have begun to answer those questions using photometric data (Mao et al. 2022) and age-sensitive spectral indices (Wu et al. 2018b; Sobral et al. 2022), but not much effort has been put toward understanding this evolution from the SFH of individual galaxies. Another interesting comparison would be to compare our SFHs to those derived from simulation using Proportional Counter Array analysis (e.g., Sparre et al. 2015).

This SFH census of a representative sample of ∼3000 massive galaxies using two state-of-the-art Bayesian modeling tools will set the benchmark at $z \sim 1$. It is a *cosmic midpoint* in time, providing a stepping stone to future spectroscopic studies of high-redshift galaxies (e.g., from JWST/NIRSpec, VLT/MOONS (Maiolino et al. 2020), or Subaru/PFS (Greene et al. 2022). By including two independent sets of models, we hope that this intermediate redshift study would be a link to other similar studies and help connect our understanding of the evolution of stellar mass growth and assembly in galaxies from cosmic noon and beyond to the present-day Universe.

Acknowledgments

R.B. and Y.K. gratefully acknowledge funding for project KA2019-105551 provided by the Robert C. Smith Fund and the Betsy R. Clark Fund of The Pittsburgh Foundation. R.B. acknowledges support from the Research Corporation for Scientific Advancement (RCSA) Cottrell Scholar Award ID No. 27587. R.B. and Y.K. also acknowledge support from NSF grant No. AST-2144314. A.G. acknowledges support from INAF-Minigrant-2022 "LEGA-C" 1.05.12.04.01. This research was supported in part by the University of Pittsburgh Center for Research Computing, RRID:SCR_022735, through the resources provided. Specifically, this work used the H2P cluster, which is supported by NSF award No. OAC-2117681. We specifically acknowledge the assistance of Prof. Kim Wong in setting up the framework at the cluster. Y.K. thanks Brett Andrews, Alan Pearl, David Setton, and Biprateep Dey for their constructive feedback and suggestions that greatly improved this work.

This work made extensive use of the publicly available tools `Bagpipes` (Carnall et al. 2018; https://bagpipes.readthedocs.io/en/latest/), `Prospector` (Johnson & Leja 2017; Johnson et al. 2021; https://prospect.readthedocs.io/en/latest/), Python programming language (van Rossum 1995; https://www.python.org), astropy (Astropy Collaboration et al. 2013; https://pypi.org/project/astropy/), matplotlib (Hunter 2007; https://pypi.org/project/matplotlib/), NumPy (Harris et al. 2020; https://pypi.org/project/numpy/), SciPy (Virtanen et al. 2020; https://pypi.org/project/SciPy/).

Appendix

Our primary spectrophotometric analysis was conducted on deep LEGA-C spectra with *BvrizYJ* broadband photometric data. To investigate whether this modeling choice impacts our final results, we fit the full LEGA-C primary sample with two more flavors in `Bagpipes`: (1) spectra + *vriz* bands and (2) spectra + 20 photometric bands (from *B* to 24 μm as described in Section 2.1). We compare the median t_{10}, t_{10}, and t_{90} formation times from these flavors with those presented in this paper from `Bagpipes` and `Prospector` using *BvrizYJ* bands only in Figure A1. Error bars represent the population scatter within the samples of that mass bin. It is evident that the derived formation times do not depend strongly on the photometric information provided to the modeling.

The population scatter is higher for earlier formation times compared to later ones with `Prospector` t_{10} dominated by the priors on the very first time bin. For the quiescent population, we do see the highest variation in the lowest mass bin of $10.5 < \log(M/M_{\odot}) < 11$, primarily driven by the low number of samples (∼290) in that mass range.

Figure A2 is an extended version of Figure 5 and shows SFHs of the quiescent and star-forming populations combined in the other two low stellar mass bins, e.g., $10.5 < \log(M_{*}/M_{\odot}) < 11$ and $11 < \log(M_{*}/M_{\odot}) < 11.5$. All symbols and labels are the same as those in Figure 5. The top two rows show the lowest mass bin for the quiescent and star-forming populations, whereas the bottom two rows show middle mass bins. Note that the vertical axis limits of SFHs in units of solar mass per year are different for the two populations to zoom into the features that are prominent in the sSFR plane.

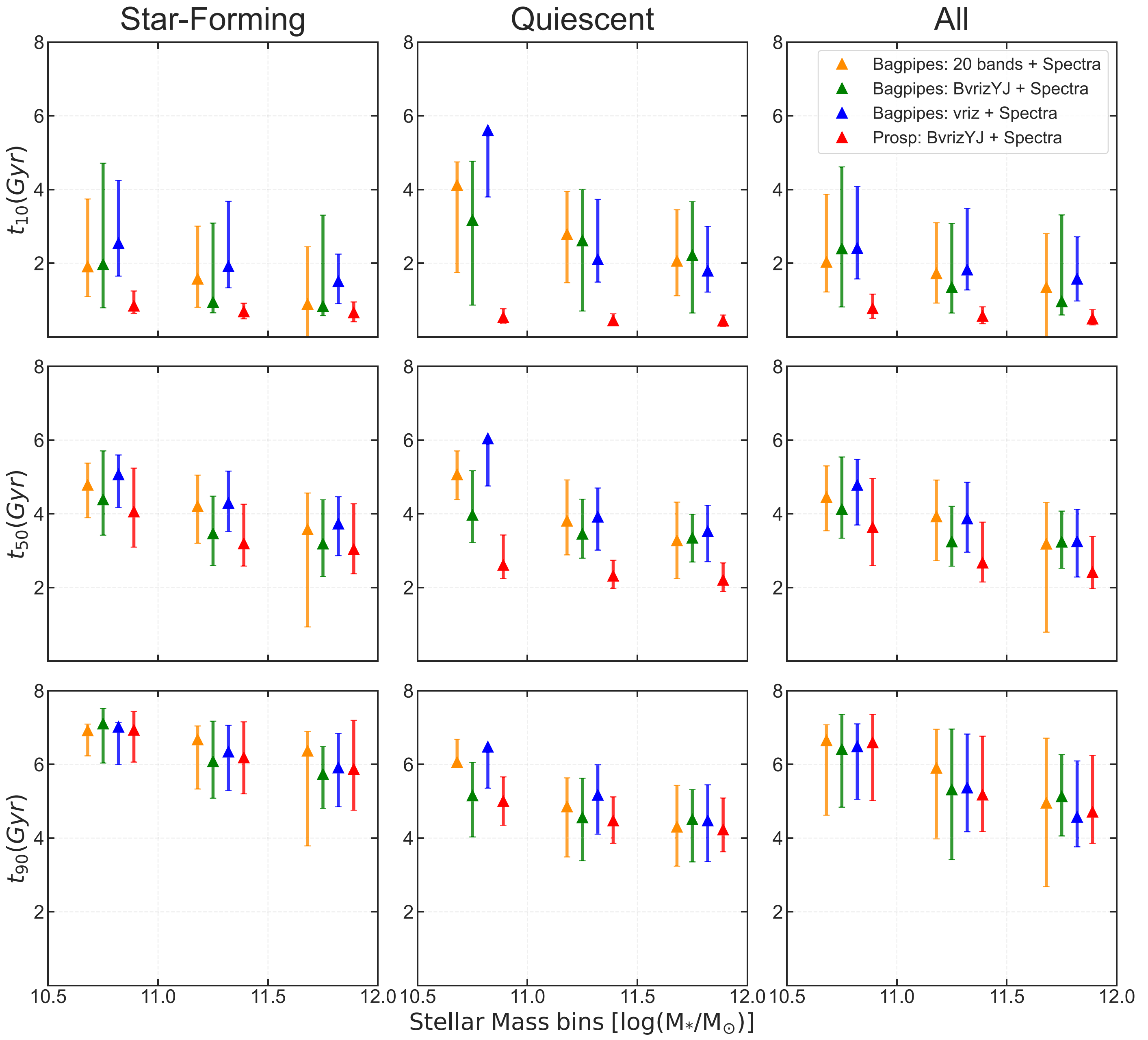

Figure A1. Comparison of 10% (top row), 50% (middle row), and 90% (bottom row) formation times for star-forming (left), quiescent (center), and all (right) galaxies from different flavors of spectrophotometric runs using `Bagpipes` and `Prospector`. Our results are robust to the photometric information provided in the fits and are defined by the high-resolution spectral information. Error bars represent the 16th–84th percentile ranges.

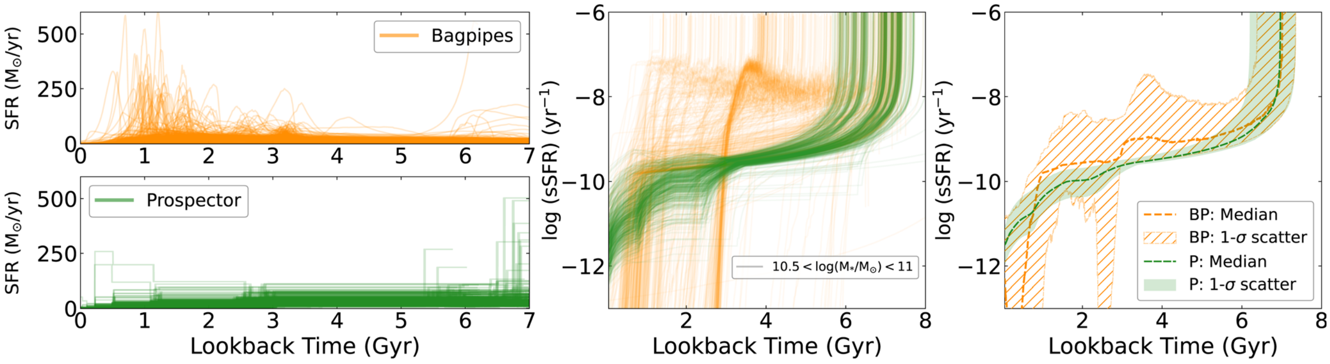

(a) Quiescent

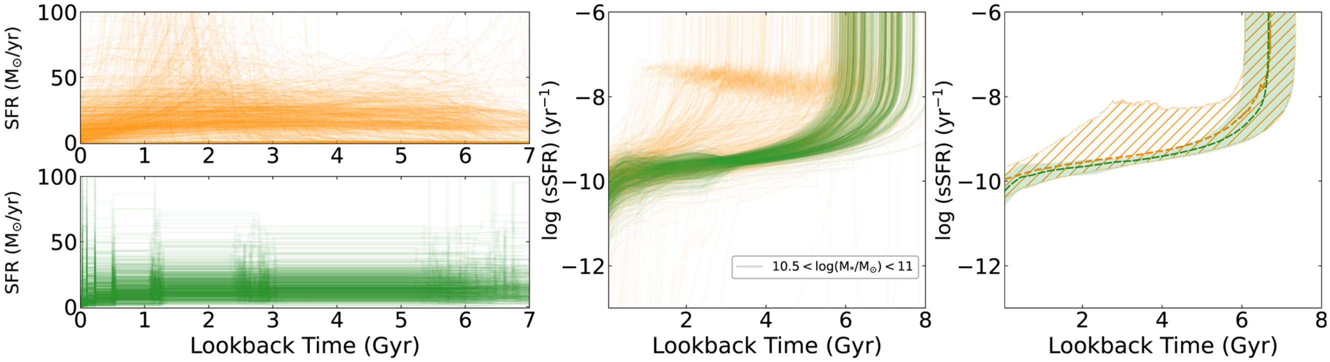

(b) Star-forming

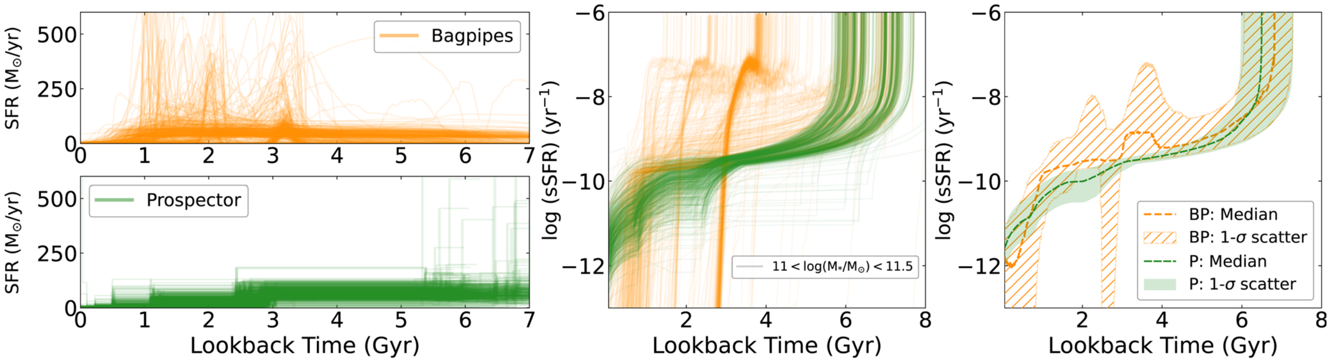

(a) Quiescent

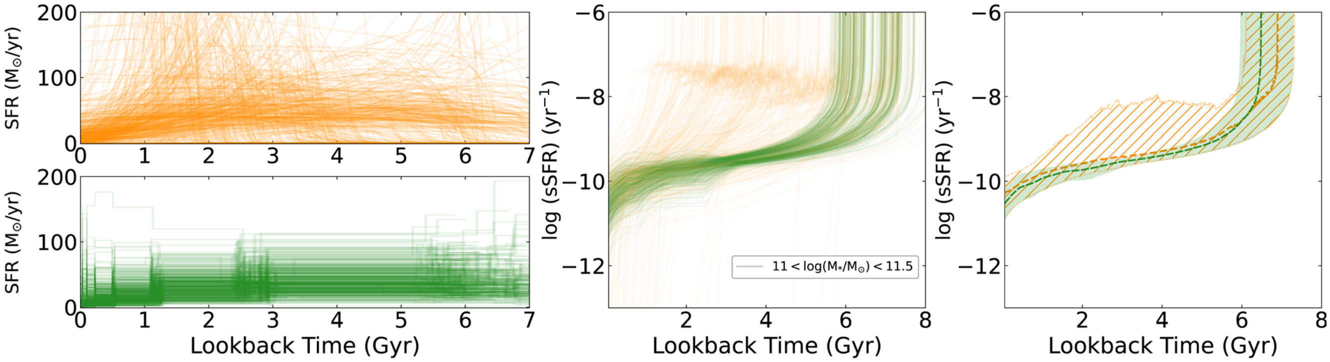

(b) Star-forming

Figure A2. Extended version of Figure 5 showing recovered SFHs of lower stellar mass galaxies for `Bagpipes` and `Prospector` in SFR ($M_\odot$ yr^{-1}) and log(sSFR) (yr^{-1}) plane. The top two rows show galaxies in the lowest stellar mass bin $10.5 < \log(M_*/M_\odot) < 11$ for quiescent (a) and star-forming (b) samples. Similarly, the bottom two row shows the same for galaxies in the $11 < \log(M_*/M_\odot) < 11.5$ stellar mass bin. Note that the vertical axis limits of SFHs are different for the two populations to zoom into the features that are prominent in the sSFR plane.

ORCID iDs

Yasha Kaushal https://orcid.org/0000-0003-4382-4467
Angelos Nersesian https://orcid.org/0000-0001-6843-409X
Rachel Bezanson https://orcid.org/0000-0001-5063-8254
Arjen van der Wel https://orcid.org/0000-0002-5027-0135
Joel Leja https://orcid.org/0000-0001-6755-1315
Adam Carnall https://orcid.org/0000-0002-1482-5818
Anna Gallazzi https://orcid.org/0000-0002-9656-1800
Stefano Zibetti https://orcid.org/0000-0003-1734-8356
Gourav Khullar https://orcid.org/0000-0002-3475-7648
Marijn Franx https://orcid.org/0000-0002-8871-3026
Adam Muzzin https://orcid.org/0000-0002-9330-9108
Anna de Graaff https://orcid.org/0000-0002-2380-9801
Camilla Pacifici https://orcid.org/0000-0003-4196-0617
Katherine E. Whitaker https://orcid.org/0000-0001-7160-3632
Eric F. Bell https://orcid.org/0000-0002-5564-9873
Marco Martorano https://orcid.org/0000-0003-2373-0404

References

Abramson, L. E., Gladders, M. D., Dressler, A., et al. 2015, ApJL, 801, L12
Astropy Collaboration, Robitaille, T. P., Tollerud, E. J., et al. 2013, A&A, 558, A33
Aufort, G., Ciesla, L., Pudlo, P., & Buat, V. 2020, A&A, 635, A136
Behroozi, P., Wechsler, R. H., Hearin, A. P., & Conroy, C. 2019, MNRAS, 488, 3143
Behroozi, P. S., Wechsler, R. H., & Conroy, C. 2013, ApJ, 770, 57
Bell, E. F., Wolf, C., Meisenheimer, K., et al. 2004, ApJ, 608, 752
Belli, S., Contursi, A., & Davies, R. I. 2018, MNRAS, 478, 2097
Belli, S., Newman, A. B., & Ellis, R. S. 2014, ApJ, 783, 117
Beverage, A. G., Kriek, M., Conroy, C., et al. 2023, ApJ, 948, 140
Bezanson, R., van der Wel, A., Straatman, C., et al. 2018, ApJL, 868, L36
Bowman, W. P., Zeimann, G. R., Nagaraj, G., et al. 2020, ApJ, 899, 7
Bruzual, G., & Charlot, S. 2003, MNRAS, 344, 1000
Calvi, R., Vulcani, B., Poggianti, B. M., et al. 2018, MNRAS, 481, 3456
Cappellari, M. 2017, MNRAS, 466, 798
Carnall, A. C., Leja, J., Johnson, B. D., et al. 2019a, ApJ, 873, 44
Carnall, A. C., McLure, R. J., Dunlop, J. S., et al. 2019b, MNRAS, 490, 417
Carnall, A. C., McLure, R. J., Dunlop, J. S., et al. 2022, ApJ, 929, 131
Carnall, A. C., McLure, R. J., Dunlop, J. S., et al. 2023a, Natur, 619, 716
Carnall, A. C., McLeod, D. J., McLure, R. J., et al. 2023b, MNRAS, 520, 3974
Carnall, A. C., McLure, R. J., Dunlop, J. S., & Davé, R. 2018, MNRAS, 480, 4379
Chabrier, G. 2003, PASP, 115, 763
Charlot, S., & Fall, S. M. 2000, ApJ, 539, 718
Chauke, P., van der Wel, A., Pacifici, C., et al. 2018, ApJ, 861, 13
Chaves-Montero, J., & Hearin, A. 2020, MNRAS, 495, 2088
Chevallard, J., & Charlot, S. 2016, MNRAS, 462, 1415
Chevallard, J., Curtis-Lake, E., Charlot, S., et al. 2019, MNRAS, 483, 2621
Choi, J., Conroy, C., Moustakas, J., et al. 2014, ApJ, 792, 95
Cid Fernandes, R. 2007, in IAU Symp. 241, Stellar Populations as Building Blocks of Galaxies, ed. A. Vazdekis & R. Peletier (Cambridge: Cambridge Univ. Press), 461
Cid Fernandes, R., Mateus, A., Sodré, L., Stasińska, G., & Gomes, J. M. 2005, MNRAS, 358, 363
Ciesla, L., Elbaz, D., & Fensch, J. 2017, A&A, 608, A41
Citro, A., Pozzetti, L., Moresco, M., & Cimatti, A. 2016, A&A, 592, A19
Cohn, J. D. 2018, MNRAS, 478, 2291
Conroy, C., Gunn, J. E., & White, M. 2009, ApJ, 699, 486
Cullen, F., McLure, R. J., Dunlop, J. S., et al. 2019, MNRAS, 487, 2038
Davé, R., Anglés-Alcázar, D., Narayanan, D., et al. 2019, MNRAS, 486, 2827
Diemer, B., Sparre, M., Abramson, L. E., & Torrey, P. 2017, ApJ, 839, 26
Draine, B. T., & Li, A. 2007, ApJ, 657, 810
Dutton, A. A., Conroy, C., van den Bosch, F. C., Prada, F., & More, S. 2010, MNRAS, 407, 2
Dye, S. 2008, MNRAS, 389, 1293
Elahi, P. J., Power, C., Lagos, C. d. P., Poulton, R., & Robotham, A. S. G. 2018, MNRAS, 477, 616
Estrada-Carpenter, V., Papovich, C., Momcheva, I., et al. 2020, ApJ, 898, 171
Falcón-Barroso, J., Sánchez-Blázquez, P., Vazdekis, A., et al. 2011, A&A, 532, A95
Ferland, G. J., Porter, R. L., van Hoof, P. A. M., et al. 2013, RMxAA, 49, 137
Feroz, F., & Hobson, M. P. 2008, MNRAS, 384, 449
Feroz, F., Hobson, M. P., Cameron, E., & Pettitt, A. N. 2019, OJAp, 2, 10
Feroz, F., & Skilling, J. 2013, in AIP Conf. Proc. 1553, 32nd Int. Workshop on Bayesian Inference and Maximum Entropy Methods in Science and Engineering, ed. U. von Toussaint (Melville, NY: AIP), 106
Ferreras, I., Pasquali, A., Pirzkal, N., et al. 2019, MNRAS, 486, 1358
Feulner, G., Goranova, Y., Drory, N., Hopp, U., & Bender, R. 2005, MNRAS, 358, L1
Forrest, B., Marsan, Z. C., Annunziatella, M., et al. 2020, ApJ, 903, 47
Franx, M., van Dokkum, P. G., Förster Schreiber, N. M., et al. 2008, ApJ, 688, 770
Gallazzi, A., Brinchmann, J., Charlot, S., & White, S. D. M. 2008, MNRAS, 383, 1439
Gallazzi, A., Charlot, S., Brinchmann, J., & White, S. D. M. 2006, MNRAS, 370, 1106
Gladders, M. D., Oemler, A., Dressler, A., et al. 2013, ApJ, 770, 64
Graves, G. J., Faber, S. M., & Schiavon, R. P. 2009, ApJ, 698, 1590
Greene, J., Bezanson, R., Ouchi, M., & Silverman, J. 2022, arXiv:2206.14908
Hamadouche, M. L., Carnall, A. C., McLure, R. J., et al. 2023, MNRAS, 521, 5400
Harris, C. R., Millman, K. J., van der Walt, S. J., et al. 2020, Natur, 585, 357
Hill, A. R., Muzzin, A., Franx, M., & Marchesini, D. 2017a, ApJL, 849, L26
Hill, A. R., Muzzin, A., Franx, M., et al. 2017b, ApJ, 837, 147
Hunter, J. D. 2007, CSE, 9, 90
Ibarra-Medel, H. J., Sánchez, S. F., Avila-Reese, V., et al. 2016, MNRAS, 463, 2799
Ilbert, O., Arnouts, S., Le Floc'h, E., et al. 2015, A&A, 579, A2
Iyer, K. 2019, AAS Meeting, 233, 429.05
Iyer, K., & Gawiser, E. 2017, ApJ, 838, 127
Iyer, K. G., Tacchella, S., Genel, S., et al. 2020, MNRAS, 498, 430
Johnson, B., & Leja, J. 2017, Bd-J/Prospector: Initial Release, v0.1, Zenodo, doi:10.5281/zenodo.1116491
Johnson, B. D., Leja, J., Conroy, C., & Speagle, J. S. 2021, ApJS, 254, 22
Kauffmann, G., White, S. D. M., Heckman, T. M., et al. 2004, MNRAS, 353, 713
Khullar, G., Bayliss, M. B., Gladders, M. D., et al. 2022, ApJ, 934, 177
Kriek, M., & Conroy, C. 2013, ApJL, 775, L16
Kriek, M., Shapley, A. E., Reddy, N. A., et al. 2015, ApJS, 218, 15
Kroupa, P. 2001, MNRAS, 322, 231
Labbé, I., van Dokkum, P., Nelson, E., et al. 2023, Natur, 616, 266
Le Fevre, O., Saisse, M., Mancini, D., et al. 2000, Proc. SPIE, 4008, 546
Leitner, S. N. 2012, ApJ, 745, 149
Leja, J., Carnall, A. C., Johnson, B. D., Conroy, C., & Speagle, J. S. 2019, ApJ, 876, 3
Leja, J., Johnson, B. D., Conroy, C., van Dokkum, P. G., & Byler, N. 2017, ApJ, 837, 170
Looser, T. J., D'Eugenio, F., Maiolino, R., et al. 2023, arXiv:2302.14155
Lower, S., Narayanan, D., Leja, J., et al. 2020, ApJ, 904, 33
Madau, P., & Dickinson, M. 2014, ARA&A, 52, 415
Maiolino, R., Cirasuolo, M., Afonso, J., et al. 2020, Msngr, 180, 24
Maltby, D. T., Almaini, O., Wild, V., et al. 2018, MNRAS, 480, 381
Mao, Z., Kodama, T., Pérez-Martínez, J. M., et al. 2022, A&A, 666, A141
Martins, L. P. 2021, in IAU Symp. 359, Galaxy Evolution and Feedback across Different Environments, ed. T. Storchi Bergmann, W. Forman, R. Overzier, & R. Riffel (Cambridge: Cambridge Univ. Press), 386
McDermid, R. M., Alatalo, K., Blitz, L., et al. 2015, MNRAS, 448, 3484
McKinney, J., Finnerty, L., Casey, C. M., et al. 2023, ApJL, 946, L39
McLure, R. J., Pentericci, L., Cimatti, A., et al. 2018, MNRAS, 479, 25
Mortlock, A., McLure, R. J., Bowler, R. A. A., et al. 2017, MNRAS, 465, 672
Muzzin, A. 2017, Early Stages of Galaxy Cluster Formation: Mergers, Protoclusters, and Star Formation in Overdense Environments (Garching: ESO), 24
Muzzin, A., Marchesini, D., Stefanon, M., et al. 2013, ApJS, 206, 8
Muzzin, A., Marchesini, D., Stefanon, M., et al. 2013, ApJ, 777, 18
Nanayakkara, T., Glazebrook, K., Jacobs, C., et al. 2023, ApJL, 947, L26
Nelan, J. E., Smith, R. J., Hudson, M. J., et al. 2005, ApJ, 632, 137
Nelson, D., Springel, V., Pillepich, A., et al. 2019, ComAC, 6, 2
Nersesian, A., van der Wel, A., Gallazzi, A., et al. 2023, A&A, in press
Newman, J. A., Cooper, M. C., Davis, M., et al. 2013, ApJS, 208, 5
Ocvirk, P., Pichon, C., Lançon, A., & Thiébaut, E. 2006, MNRAS, 365, 46
Olsen, C., Gawiser, E., Iyer, K., et al. 2021, ApJ, 913, 45
Pacifici, C., Charlot, S., Blaizot, J., & Brinchmann, J. 2012, MNRAS, 421, 2002

Pacifici, C., Iyer, K. G., Mobasher, B., et al. 2023, ApJ, 944, 141
Pacifici, C., Oh, S., Oh, K., Lee, J., & Yi, S. K. 2016a, ApJ, 824, 45
Pacifici, C., Kassin, S. A., Weiner, B. J., et al. 2016b, ApJ, 832, 79
Panter, B., Jimenez, R., Heavens, A. F., & Charlot, S. 2007, MNRAS, 378, 1550
Pforr, J., Maraston, C., & Tonini, C. 2012, MNRAS, 422, 3285
Rudie, G. C., Steidel, C. C., Trainor, R. F., et al. 2012, ApJ, 750, 67
Sánchez-Blázquez, P., Ocvirk, P., Gibson, B. K., Pérez, I., & Peletier, R. F. 2011, MNRAS, 415, 709
Schawinski, K., Urry, C. M., Simmons, B. D., et al. 2014, MNRAS, 440, 889
Schiavon, R. P., Faber, S. M., Konidaris, N., et al. 2006, ApJL, 651, L93
Schreiber, C., Elbaz, D., Pannella, M., et al. 2016, A&A, 589, A35
Shamshiri, S., Thomas, P. A., Henriques, B. M., et al. 2015, MNRAS, 451, 2681
Sharma, S., Hayden, M. R., Bland-Hawthorn, J., et al. 2021, MNRAS, 506, 1761
Simha, V., Weinberg, D. H., Conroy, C., et al. 2014, arXiv:1404.0402
Siudek, M., Małek, K., Scodeggio, M., et al. 2017, A&A, 597, A107
Skilling, J. 2006, BayAn, 1, 833
Smethurst, R. J., Lintott, C. J., Simmons, B. D., et al. 2015, MNRAS, 450, 435
Sobral, D., van der Wel, A., Bezanson, R., et al. 2022, ApJ, 926, 117
Sparre, M., Hayward, C. C., Springel, V., et al. 2015, MNRAS, 447, 3548
Speagle, J. S. 2020, MNRAS, 493, 3132
Steidel, C. C., Rudie, G. C., Strom, A. L., et al. 2014, ApJ, 795, 165
Straatman, C. M. S., van der Wel, A., Bezanson, R., et al. 2018, ApJS, 239, 27
Strom, A. L., Steidel, C. C., Rudie, G. C., et al. 2017, ApJ, 836, 164
Suess, K. A., Leja, J., Johnson, B. D., et al. 2022a, ApJ, 935, 146
Suess, K. A., Kriek, M., Bezanson, R., et al. 2022b, ApJ, 926, 89
Tacchella, S., Conroy, C., Faber, S. M., et al. 2022, ApJ, 926, 134
Taylor, E. N., Hopkins, A. M., Baldry, I. K., et al. 2015, MNRAS, 446, 2144
Taylor, L., Bezanson, R., van der Wel, A., et al. 2022, ApJ, 939, 90
Thomas, D., Maraston, C., Bender, R., & Mendes de Oliveira, C. 2005, ApJ, 621, 673
Thomas, D., Maraston, C., Schawinski, K., Sarzi, M., & Silk, J. 2010, MNRAS, 404, 1775
Thomas, R., Le Fèvre, O., Scodeggio, M., et al. 2017, A&A, 602, A35
Tojeiro, R., Wilkins, S., Heavens, A. F., Panter, B., & Jimenez, R. 2009, ApJS, 185, 1
Torrey, P., Vogelsberger, M., Hernquist, L., et al. 2018, MNRAS, 477, L16
van der Wel, A., Bezanson, R., D'Eugenio, F., et al. 2021, ApJS, 256, 44
van der Wel, A., Noeske, K., Bezanson, R., et al. 2016, ApJS, 223, 29
van der Wel, A., van Houdt, J., Bezanson, R., et al. 2022, ApJ, 936, 9
van Houdt, J., van der Wel, A., Bezanson, R., et al. 2021, ApJ, 923, 11
van Rossum, G. 1995, CWI Technical Report, CS-R9526, Centrum Wiskunde & Informatica https://ir.cwi.nl/pub/5007/05007D.pdf
Virtanen, P., Gommers, R., Oliphant, T. E., et al. 2020, NatMe, 17, 261
Vulcani, B., Bamford, S. P., Häußler, B., et al. 2014, MNRAS, 441, 1340
Wake, D. A., van Dokkum, P. G., & Franx, M. 2012, ApJL, 751, L44
Webb, K., Balogh, M. L., Leja, J., et al. 2020, MNRAS, 498, 5317
Weisz, D. R., Dalcanton, J. J., Williams, B. F., et al. 2011, ApJ, 739, 5
Weisz, D. R., Skillman, E. D., Cannon, J. M., et al. 2008, ApJ, 689, 160
Wild, V., Almaini, O., Dunlop, J., et al. 2016, MNRAS, 463, 832
Wu, P.-F., van der Wel, A., Bezanson, R., et al. 2018a, ApJ, 868, 37
Wu, P.-F., van der Wel, A., Gallazzi, A., et al. 2018b, ApJ, 855, 85
Wuyts, S., Franx, M., Cox, T. J., et al. 2009, ApJ, 696, 348
Zahid, H. J., Sohn, J., & Geller, M. J. 2018, ApJ, 859, 96